

1 **Virological characteristics of the SARS-CoV-2 Omicron EG.5.1 variant**

2

3 Shuheï Tsujino^{1#}, Sayaka Deguchi^{2#}, Tomo Nomai^{3#}, Miguel Padilla-Blanco^{4,5},
4 Arnon Plianchaisuk^{6#}, Lei Wang^{7,8#}, MST Monira Begum^{9#}, Keiya Uriu^{6,10#}, Keita
5 Mizuma^{11,12,13,14}, Naganori Nao^{11,12,13,14}, Isshu Kojima^{11,12,13,14}, Tomoya
6 Tsubo^{11,12,13,14}, Jingshu Li^{11,12,13,14}, Yasufumi Matsumura¹⁵, Miki Nagao¹⁵,
7 Yoshitaka Oda^{7,8}, Masumi Tsuda^{7,8}, Yuki Anraku³, Shunsuke Kita³, Hisano
8 Yajima¹⁶, Kaori Sasaki-Tabata¹⁷, Ziyi Guo⁶, Alfredo A Hinay Jr.⁶, Kumiko
9 Yoshimatsu¹⁸, Yuki Yamamoto¹⁹, Tetsuharu Nagamoto¹⁹, Hiroyuki Asakura²⁰,
10 Mami Nagashima²⁰, Kenji Sadamasu²⁰, Kazuhisa Yoshimura²⁰, Hesham
11 Nasser^{9,21}, Michael Jonathan⁹, Olivia Putri^{6,22}, Yoonjin Kim^{6,23}, Luo Chen^{6,24},
12 Rigel Suzuki^{1,25}, Tomokazu Tamura^{1,12,25}, Katsumi Maenaka^{3,26,27,28}, The
13 Genotype to Phenotype Japan (G2P-Japan) Consortium, Takashi Irie²⁹, Keita
14 Matsuno^{11,12,13,14}, Shinya Tanaka^{7,8}, Jumpei Ito^{6,10,30}, Terumasa Ikeda^{9*}, Kazuo
15 Takayama^{2,31*}, Jiri Zahradnik^{4*}, Takao Hashiguchi^{16,32*}, Takasuke
16 Fukuhara^{1,12,25,31,33*}, Kei Sato^{6,10,24,30,32,34,35*}

17

18 ¹ Department of Microbiology and Immunology, Faculty of Medicine, Hokkaido
19 University, Sapporo, Japan.

20 ² Center for iPS Cell Research and Application (CiRA), Kyoto University, Kyoto,
21 Japan

22 ³ Laboratory of Biomolecular Science and Center for Research and Education
23 on Drug Discovery, Faculty of Pharmaceutical Sciences, Hokkaido University,
24 Sapporo, Japan

25 ⁴ First Medical Faculty at Biocev, Charles University, Vestec-Prague, Czechia

26 ⁵ Departamento de Farmacia, Facultad de Ciencias de la Salud, Universidad
27 Cardenal Herrera-CEU (UCH-CEU), CEU Universities, Valencia, Spain

28 ⁶ Division of Systems Virology, Department of Microbiology and Immunology,
29 The Institute of Medical Science, The University of Tokyo, Tokyo, Japan

30 ⁷ Department of Cancer Pathology, Faculty of Medicine, Hokkaido University,
31 Sapporo, Japan

32 ⁸ Institute for Chemical Reaction Design and Discovery (WPI-ICReDD),
33 Hokkaido University, Sapporo, Japan

34 ⁹ Division of Molecular Virology and Genetics, Joint Research Center for Human
35 Retrovirus infection, Kumamoto University, Kumamoto, Japan

36 ¹⁰ Graduate School of Medicine, The University of Tokyo, Tokyo, Japan

37 ¹¹ Division of Risk Analysis and Management, International Institute for Zoonosis
38 Control, Hokkaido University, Sapporo, Japan

39 ¹² One Health Research Center, Hokkaido University, Sapporo, Japan

40 ¹³ International Collaboration Unit, International Institute for Zoonosis Control,
41 Hokkaido University, Sapporo, Japan

42 ¹⁴ Institute for Vaccine Research and Development (IVReD), Hokkaido
43 University, Sapporo, Japan

44 ¹⁵ Department of Clinical Laboratory Medicine, Graduate School of Medicine,
45 Kyoto University, Kyoto, Japan

46 ¹⁶ Laboratory of Medical Virology, Institute for Life and Medical Sciences, Kyoto
47 University, Kyoto, Japan

48 ¹⁷ Department of Medicinal Sciences, Graduate School of Pharmaceutical
49 Sciences, Kyushu University, Fukuoka, Japan

50 ¹⁸ Institute for Genetic Medicine, Hokkaido University, Sapporo, Japan

51 ¹⁹ HiLung Inc., Kyoto, Japan

52 ²⁰ Tokyo Metropolitan Institute of Public Health, Tokyo, Japan

53 ²¹ Department of Clinical Pathology, Faculty of Medicine, Suez Canal University,
54 Ismailia, Egypt

55 ²² Department of Biomedicine, School of Life Sciences, Indonesia International
56 Institute for Life Sciences (i3L), Jakarta, Indonesia

57 ²³ Department of Life Sciences, Faculty of Natural Science, Imperial College
58 London, London, United Kingdom

59 ²⁴ Graduate School of Frontier Sciences, The University of Tokyo, Kashiwa,
60 Japan

61 ²⁵ Institute for Vaccine Research and Development (IVReD), Hokkaido
62 University, Sapporo, Japan

63 ²⁶ Institute for Vaccine Research and Development, HU-IVReD, Hokkaido
64 University, Sapporo, Japan

65 ²⁷ Global Station for Biosurfaces and Drug Discovery, Hokkaido University,
66 Sapporo, Japan

67 ²⁸ Division of Pathogen Structure, International Institute for Zoonosis Control,
68 Hokkaido University, Sapporo, Japan

69 ²⁹ Institute of Biomedical and Health Sciences, Hiroshima University, Hiroshima,
70 Japan.

71 ³⁰ International Research Center for Infectious Diseases, The Institute of Medical
72 Science, The University of Tokyo, Tokyo, Japan

73 ³¹ AMED-CREST, Japan Agency for Medical Research and Development
74 (AMED), Tokyo, Japan

75 ³² CREST, Japan Science and Technology Agency, Kawaguchi, Japan

76 ³³ Laboratory of Virus Control, Research Institute for Microbial Diseases, Osaka
77 University, Suita, Japan

78 ³⁴ International Vaccine Design Center, The Institute of Medical Science, The
79 University of Tokyo, Tokyo, Japan

80 ³⁵ Collaboration Unit for Infection, Joint Research Center for Human Retrovirus
81 infection, Kumamoto University, Kumamoto, Japan

82 #These authors contributed equally

83

84 *Corresponding authors:

85 ikedat@kumamoto-u.ac.jp (Terumasa Ikeda),

86 kazuotakayama@cira.kyoto-u.ac.jp (Kazuo Takayama),

87 jiri.zahradnik2@gmail.com (Jiri Zahradnik),

88 hashiguchi.takao.1a@kyoto-u.ac.jp (Takao Hashiguchi),

89 fukut@pop.med.hokudai.ac.jp (Takasuke Fukuhara),

90 KeiSato@g.ecc.u-tokyo.ac.jp (Kei Sato)

91

92 **Short title:** Characteristics of SARS-CoV-2 EG.5.1 (37/50 characters)

93

94 **Keywords:** SARS-CoV-2; COVID-19; Omicron; EG.5.1; pathogenicity; ORF9b

95 **Abstract** (142/150 words)

96 In middle-late 2023, a sublineage of SARS-CoV-2 Omicron XBB, EG.5.1 (a
97 progeny of XBB.1.9.2), is spreading rapidly around the world. Here, we
98 performed multiscale investigations to reveal virological features of newly
99 emerging EG.5.1 variant. Our phylogenetic-epidemic dynamics modeling
100 suggested that two hallmark substitutions of EG.5.1, S:F456L and ORF9b:I5T,
101 are critical to the increased viral fitness. Experimental investigations addressing
102 the growth kinetics, sensitivity to clinically available antivirals, fusogenicity and
103 pathogenicity of EG.5.1 suggested that the virological features of EG.5.1 is
104 comparable to that of XBB.1.5. However, the cryo-electron microscopy reveals
105 the structural difference between the spike proteins of EG.5.1 and XBB.1.5. We
106 further assessed the impact of ORF9b:I5T on viral features, but it was almost
107 negligible at least in our experimental setup. Our multiscale investigations
108 provide the knowledge for understanding of the evolution trait of newly emerging
109 pathogenic viruses in the human population.

110 Introduction

111 XBB is a recombinant SARS-CoV-2 Omicron lineage emerged in the summer of
112 2022¹. As of October 2023, some XBB sublineages bearing the F486P
113 substitution in the spike protein (S; S:F486P), such as XBB.1.5 and XBB.1.16,
114 have become predominant worldwide (<https://nextstrain.org/>). Because S:F486P
115 significantly increased pseudovirus infectivity², it is assumed that the spread of
116 F486P-bearing XBB subvariants is attributed to the increased infectivity from
117 S:F486P.

118 Since July 2023, EG.5.1 (also known as XBB.1.9.2.5.1) has rapidly
119 spread in some Asian and North American countries. On August 9, 2023, the
120 WHO classified EG.5 as a variant of interest³. In fact, our recent study showed
121 that EG.5.1 exhibits a greater effective reproduction number (R_e) compared with
122 XBB.1.5, XBB.1.16, and its parental lineage (XBB.1.9.2)⁴. These observations
123 suggest that EG.5. has the potential to spread globally and outcompete these
124 XBB subvariants.

125 EG.5.1 bears two evolutionary characteristic mutations, S:F456L and
126 ORF9b:I5T, absent in earlier predominant lineages such as XBB.1.5. These two
127 substitutions convergently occurred in multiple SARS-CoV-2 lineages
128 (<https://bloombio.github.io/SARS2-mut-fitness/>). Importantly, it has been
129 reported that convergent mutations tend to increase viral fitness—the ability of
130 virus to spread in the human population, quantified with the effective
131 reproduction number (R_e)^{5,6}. In fact, we have shown that the S:F456L in EG.5.1
132 confers resistance to the humoral immunity induced by XBB breakthrough
133 infection (BTI)⁴. This result suggests that S:F456L contributes to the increased
134 viral fitness of EG.5.1 by enhancing immune evasion from the humoral immunity
135 elicited by XBB BTI.

136 SARS-CoV-2 ORF9b is a viral antagonist that hampers the innate
137 immunity to induce type I interferon (IFN-I) production⁷⁻¹⁰. Of note, the
138 ORF9b:I5T substitution is detected in multiple lineages including XBB.1.9 and
139 EG.5.1 (<https://github.com/cov-lineages/pango-designation>), which raises a
140 possibility that the ORF9b:I5T has a crucial role in these XBB sublineages.
141 However, the impact of ORF9b:I5T on the characteristics of SARS-CoV-2
142 variants is not documented yet.

143 The R_e and immune evasive property of SARS-CoV-2 Omicron EG.5.1
144 variant have been addressed by us⁴ and other groups^{11,12}. However, mutations
145 that contribute to the increased viral fitness in EG.5.1 have been unidentified.
146 Moreover, the growth kinetics, sensitivity to clinically available antiviral
147 compounds, fusogenicity and pathogenicity of EG.5.1 remains to be addressed.
148 In this study, we elucidated the virological characteristics of SARS-CoV-2
149 Omicron EG.5.1 variant.

150 **Results**

151 **Mutations contributing to the increased viral fitness of EG.5.1**

152 Compared with XBB.1.5, EG.5.1 has two amino acid substitutions in S (S:Q52H
153 and S:F456L) and five substitutions in other proteins (**Figure 1A**). Of these,
154 S:F456L and ORF9b:I5T are documented as convergent substitutions
155 (<https://jbloomlab.github.io/SARS2-mut-fitness/>). ORF9b:I5T is already present
156 in XBB.1.9, the ancestral lineage of EG.5.1, whereas S:F456L is absent (**Figure**
157 **1A**). EG.5.1.1, a major descendant lineage of EG.5.1, has an additional
158 ORF1b:D54N substitution compared with EG.5.1 (**Figure 1A**).

159 To test whether the convergent substitutions S:F456L and ORF9b:I5T
160 have contributed to the increased viral fitness of EG.5.1, we performed
161 phylogenetic and epidemic dynamics analyses using the genome surveillance
162 data obtained from GISAID (<https://gisaid.org/>). First, we traced the occurrence
163 events of ORF9b:I5T and S:F456L substitutions throughout the diversification of
164 XBB lineages and investigate how often each substitution has occurred, which is
165 likely to indicate the effect of substitution on viral fitness (**Figure 1B**)^{5,6}. We
166 reconstructed a phylogenetic tree of XBB lineage including 248 PANGO
167 lineages. Subsequently, we inferred the state of presence or absence of
168 ORF9b:I5T and S:F456L substitutions in ancestral nodes and pinpointed where
169 each substitution occurred. We detected three and five occurrence events of
170 ORF9b:I5T and S:F456L substitutions, respectively, supporting that these
171 substitutions have occurred convergently during the XBB diversification (**Figure**
172 **1B**). Considering the evolutionary path of EG.5 lineage, the ORF9b:I5T
173 substitution occurred first in a common ancestor of XBB.1.9, XBB.1.16, and
174 XBB.1.22 lineages, which share this substitution. The S:F456L substitution
175 occurred later in the most recent common ancestor of EG.5 lineage.

176 Next, we estimated the effect of ORF9b:I5T and S:F456L substitutions
177 on viral fitness (i.e., R_e) using a Bayesian hierarchical multinomial logistic model,
178 established in our previous study⁵. This model can estimate the effect of an
179 amino acid substitution on R_e and predict the R_e of a SARS-CoV-2 variant as a
180 linear combination of the effects of individual substitutions⁵. First, we retrieved
181 amino acid substitution profiles of SARS-CoV-2 in the XBB lineage circulated in
182 the USA from December 1, 2022, to September 15, 2023, and classified the
183 SARS-CoV-2 into haplotypes, groups of viruses sharing a unique substitution
184 profile. These resulted in 470 haplotypes according to the profile of 283
185 substitutions in the 12 SARS-CoV-2 proteins. We then estimated the effect of
186 each substitution on R_e and predicted the R_e of each haplotype using our model.
187 Our modeling analysis suggests that ORF9b:I5T and S:F456L substitutions have
188 the strongest and second-strongest positive effects on R_e among the
189 substitutions we investigated, respectively (**Figure 1C, Supplementary Table 1**),
190 whereas S:Q52H and ORF1b:D54N substitutions have a weaker positive effect

191 on R_e (**Figure 1C**). Furthermore, we showed that haplotypes with ORF9b:I5T or
192 S:F456L substitutions tend to show higher R_e . In particular, haplotypes with both
193 ORF9b:I5T and S:F456L substitutions, including EG.5, EG.5.1, and FL.1.5.1
194 (XBB.1.9.1.1.5.1), exhibit the highest R_e among the haplotypes we investigated
195 (**Figure 1D, Supplementary Table 2**). FL.1.5.1 is a descendant lineage of
196 XBB.1.9 harboring S:F456L substitution which is independent of the EG.5
197 lineage. Altogether, our analyses suggest that the increased viral fitness of
198 EG.5.1 is primarily due to the ORF9b:I5T and S:F456L convergent substitutions.
199

200 **Growth kinetics of EG.5.1 and EG.5.1.1 *in vitro***

201 To investigate the growth kinetics of EG.5.1 and EG.5.1.1 in *in vitro* cell culture
202 systems, we inoculated clinical isolates of Delta, XBB.1.5, EG.5.1, and EG.5.1.1
203 into multiple cell cultures. In Vero cells (**Figure 2A**), VeroE6/TMPRSS2 cells
204 (**Figure 2B**) and 293-ACE2/TMPRSS2 cells (**Figure 2C**), the replication kinetics
205 of Delta and XBB1.5 were comparable. On the other hand, the growth kinetics of
206 EG.5.1 and EG.5.1.1 in these three cell cultures were significantly lower than
207 that of XBB.1.5 (**Figures 2A-2C**). In Calu-3 cells (**Figure 2D**) and airway
208 organoid-derived air-liquid interface (ALI) model (**Figure 2E**), while the
209 replication kinetics of Delta was greater than that of XBB.1.5, those of XBB.1.5,
210 EG.5.1, and EG.5.1.1 were comparable. In human iPSC-derived alveolar
211 epithelial cells (**Figure 2F**), the replication kinetics of XBB.1.5 was slightly
212 decreased compared with Delta, and EG.5.1 replication was lower than that of
213 XBB.1.5. EG.5.1.1 showed the poorest replication capacity among the variants
214 tested.

215

216 **Sensitivity of EG.5.1 and EG.5.1.1 to antiviral drugs**

217 We then evaluated the sensitivity of EG.5.1 and EG.5.1.1 to three antiviral drugs,
218 Remdesivir, Ensitrelvir, and Nirmatrelvir (also known as PF-07321332). Clinical
219 isolates of Delta and XBB.1.5 were used as controls. These viruses were
220 inoculated into human iPSC-derived lung organoids, a physiologically relevant
221 model, and treated with three antiviral drugs. Nirmatrelvir showed the strongest
222 antiviral effects and no differences in antiviral efficacy were observed between
223 four variants ($EC_{50} = 0.41$ nM, 0.62 nM, 0.88 nM, and 0.82 nM for Delta, XBB.1.5,
224 EG.5.1, and EG.5.1.1, respectively) (**Figure 3**). Similarly, Remdesivir and
225 Ensitrelvir showed significant antiviral effects to these four isolates tested
226 (**Figure 3**).

227

228 **ACE2 binding affinity of EG.5.1 S**

229 The binding affinity of EG.5.1 S receptor binding domain (RBD) was measured
230 by yeast surface display^{7,8,10,16,19,34,36,40}. Consistent with our previous reports^{2,13},
231 the S RBD of XBB.1.5 exhibited the lowest K_D value when compared to those of

232 XBB.1 and XBB.1.16 (**Figure 4A**). Additionally, we showed that the K_D value of
233 EG.5.1 S RBD was significantly higher than that of XBB.1.5 (**Figure 4A**). Similar
234 to the observation of pseudovirus assay⁴, our data suggest that the infectious
235 potential of EG.5.1 is not greater than that of XBB.1.5.

236

237 **Fusogenicity of EG.5.1 S**

238 The fusogenicity of EG.5.1 S protein was measured by the SARS-CoV-2 S
239 protein-mediated membrane fusion assay^{1,5,14-21} using Calu-3/DSP₁₋₇ cells.
240 Compared to the XBB.1.5 S protein, the surface expression levels of the S
241 proteins of Delta, BA.2, XBB.1, and EG.5.1 were reduced, while B.1.1 S protein
242 was expressed higher on the surface of HEK293 cells (**Figure 4B**). The S:Q52H
243 and S:F456L, hallmark amino acid substitutions of EG.5.1 S, did not affect the
244 surface expression level of XBB.1.5 S (**Figure 4B**).

245 As previously reported^{1,16,17,21}, the Delta S protein exhibited the
246 greatest fusogenicity, while the BA.2 S protein exhibited the weakest
247 fusogenicity (**Figure 4C**). Also, the XBB.1 S protein exhibited comparable
248 fusogenicity to the XBB.1.5 S protein²². Here we found that the fusogenicity of
249 EG.5.1 S was comparable to that of XBB.1.5 S, and the Q52H and F456L
250 substitutions did not affect fusogenicity of XBB.1.5 S (**Figure 4C**). These results
251 suggest that the EG.5.1 S protein exhibits comparable fusogenicity to XBB.1 and
252 XBB.1.5 S proteins.

253

254 **Impact of EG.5.1 and EG.5.1.1 infection on the epithelial-endothelial barrier**

255 To assess the effects of EG.5.1 and EG.5.1.1 infection on the airway epithelial
256 and endothelial barriers, we employed an airway-on-a-chip system. The quantity
257 of viruses that infiltrates from the top channel to the bottom channel reflects the
258 capacity of viruses to breach the airway epithelial and endothelial
259 barriers^{1,5,19,22,23}. Notably, the percentage of virus that infiltrated the bottom
260 channel of the EG.5.1- and EG.5.1.1-infected airway-on-a-chip was comparable
261 to that of the XBB.1.5-infected airway-on-a-chip (**Figures 4D and 4E**). Together
262 with the findings of the S-based fusion assay (**Figure 4C**), these results suggest
263 that the fusogenicity of EG.5.1 and EG.5.1.1 is comparable to that of XBB.1.5.

264

265 **Structural characteristics of EG.5.1 S protein**

266 To gain structural insights into EG.5.1 S protein, the structures of the EG.5.1 S
267 ectodomain alone were determined by cryoelectron microscopy (cryo-EM)
268 analysis. The EG.5.1 S ectodomain was reconstructed as two closed states and
269 a 1-up state at resolutions of 2.50 Å, 2.89 Å and 3.34 Å, respectively (**Figure 5A**,
270 **Supplementary Figures 1A-B, and Supplementary Table 3**). The two closed
271 states in EG.5.1 show structural differences in the orientation of the RBD and the
272 loop structure at the protomer interface (**Figure 5A and Supplementary Figure**

273 **1C**), as observed in XBB.1 and XBB.1.5¹, therefore, these two closed states
274 were defined as closed-1 and closed-2, respectively. In addition, a 1-up state
275 was also observed in EG.5.1, which could not be observed in XBB.1 and
276 XBB.1.5. XBB variant was derived from recombination of BJ.1.1 with BM.1.1.1, a
277 descendant of BA.2.75¹, two closed and a 1-up states are observed in BA.2.75 S
278 like EG.5.1 S^{19,24}. Thus, from BA.2.75 through XBB to EG.5.1, there exist
279 conformational differences among the representative structures of the spike
280 protein of these variants. To examine the reason for transition of spike protein
281 conformation, we compared the structures of XBB.1.5 and EG.5.1²². While
282 closed-1 state of XBB.1.5 and EG.5.1 share a nearly identical overall structure,
283 the relative orientation of RBD in the closed-2 state show a minor displacement
284 (**Figure 5B**). EG.5.1 has the Q52H substitution in the NTD and the F456L
285 substitution in the RBD compared to XBB.1.5 (**Supplementary Figures 1D-E**),
286 especially the F456L substitution is located at the interface between protomers
287 in the closed-2 state (**Figure 5C**). When focusing on the interactions of F456L, in
288 XBB.1.5 S, F456 was located at a distance of 3.8 Å from P373, whereas in
289 EG.5.1, F456L and P373 exhibited a distance of 10.1 Å, thus resolving
290 hydrophobic interactions (**Figure 5C**). This structural difference suggests that
291 the closed-2 state of EG.5.1 exhibits a weaker RBD packing compared to
292 XBB.1/XBB.1.5, allowing for EG.5.1 S to more likely transit to the 1-up state. It
293 has been previously reported that the F486 residue stabilizes the 1-up
294 conformation by interacting to the up RBD^{25,26}. To verify the position of
295 amino-acid residue 486 in RBD and up RBDs of EG.5.1 S, we focused on the
296 interface between down and up RBDs in the 1-up state (**Supplementary Figure**
297 **1A**). Although the details of the interaction are unclear due to resolution
298 limitations, the P486 residue was found to be in contact with the up RBD residue,
299 suggesting that it may also contribute to the stabilization of the 1-up state
300 (**Figure 5D**).

301

302 **Virological characteristics of EG.5.1 and EG.5.1.1 *in vivo***

303 To investigate the virological features of EG.5.1 and its variant EG.5.1.1 *in vivo*,
304 clinical isolates of Delta, XBB.1.5, EG.5.1, and EG.5.1.1 (10,000 TCID₅₀) were
305 intranasally inoculated into hamsters under anesthesia. Consistent with our
306 previous studies^{1,5,15,16,19}, Delta infection resulted in weight loss (**Figure 6A, left**).
307 The body weights of the hamsters infected with XBB.1.5, EG.5.1 and EG.5.1.1
308 were comparable and significantly lower than that of uninfected hamsters
309 (**Figure 6A, left**).

310 We then analyzed the pulmonary function of infected hamsters as
311 reflected by two parameters, enhanced pause (Penh) and the ratio of time to
312 peak expiratory flow relative to the total expiratory time (Rpef). Delta infection
313 resulted in significant differences in these two respiratory parameters compared

314 to XBB.1.5 infection (**Figure 6A, middle and right**), suggesting that Delta is
315 more pathogenic than XBB.1.5. On the other hand, the Penh and Rpef values of
316 EG.5.1-, EG.5.1.1-, and XBB.1.5-infected hamsters were comparable (**Figure**
317 **6A, middle and right**), suggesting that the pathogenicity of EG.5.1 variants is
318 similar to that of XBB.1.5 in hamsters.

319 To evaluate the viral spread in infected hamsters, we routinely
320 measured the viral RNA load in the oral swab. Although the viral RNA load of
321 EG.5.1-infected hamsters were significantly higher than that of XBB.1.5-infected
322 hamster at 2 d.p.i., the EG.5.1 RNA load was acutely decreased and was
323 significantly lower than the XBB.1.5 RNA load at 5 d.p.i (**Figure 6B, left**).

324 We then compared the viral spread in the respiratory tissues. We
325 collected the lungs of infected hamsters at 2 and 5 d.p.i., and the collected
326 tissues were separated into the hilum and periphery regions. The viral RNA
327 loads in both the lung hilum and periphery regions of Delta-infected hamsters
328 were significantly higher than those of the other three Omicron subvariants. The
329 viral RNA loads in both lung regions of EG.5.1-infected hamsters were slightly
330 lower than those of XBB.1.5-infected hamsters (**Figure 6B, middle and right**).
331 In the lung hilum region, the viral RNA load of EG.5.1.1-infected hamsters were
332 comparable to that of XBB.1.5-infected hamsters at 2 and 5 d.p.i. (**Figure 6B,**
333 **middle**). However, in the lung periphery region, the EG.5.1.1 RNA load was
334 significantly lower than the XBB.1.5 RNA load (**Figure 6B, right**). These results
335 suggest that the viral spreading efficacy of EG.5.1 and EG.5.1.1 in the lung is
336 lower than that of XBB.1.5.

337 To further investigate of the viral spread in the respiratory tissues of
338 infected hamsters, we analyzed the formalin-fixed right lungs of infected
339 hamsters at 2 and 5 d.p.i. by carefully identifying the four lobules and lobar
340 bronchi sectioning each lobe along with the bronchial branches and performed
341 immunohistochemical (IHC) analysis targeting viral nucleocapsid (N) protein.
342 Consistent with our previous studies^{1,5,15-19,22}, at 2 d.p.i., the N-positive cells
343 were strongly detected in Delta-infected hamsters in the alveolar space around
344 the bronchi/bronchioles (**Figure 6C**). In the three Omicron subvariants, the
345 percentage of N-positive cells in the lungs of EG.5.1- and EG.5.1.1-infected
346 hamsters were comparable to that of XBB.1.5-infected hamsters (**Figure 6C and**
347 **Supplementary Figure 2A**). At 5 d.p.i., N-positive cells were detected in the
348 peripheral alveolar space in Delta-infected hamsters, while the N-positive areas
349 of EG.5.1-, EG.5.1.1- and XBB.1.5-infected hamsters were slightly detectable in
350 the peripheral alveolar space (**Figure 6C and Supplementary Figure 2B**).
351 There was no significant difference in the N-positive area of three Omicron
352 subvariants (**Supplementary Figures 2A and 2B**).

353

354 **Intrinsic pathogenicity of EG.5.1 and EG.5.1.1**

355 To investigate the intrinsic pathogenicity of EG.5.1 and EG.5.1.1,
356 histopathological analyses were performed according to the criteria described in
357 our previous study¹⁶. At 2 d.p.i., inflammation was limited in bronchi/bronchioles
358 in the hamsters infected with EG.5.1, EG.5.1.1 and XBB.1.5 (**Figure 6D and**
359 **Supplementary Figure 3A**). On the other hand, alveolar damage around the
360 bronchi was prominent in Delta-infected hamsters (**Figure 6D**). At 5 d.p.i.,
361 although the alveolar architecture was totally destroyed by the alveolar damage
362 or the expansion of type II pneumocytes in Delta-infected hamsters, alveolar
363 architecture was preserved in the three Omicron subvariant-infected hamsters
364 (**Figures 6D, 6E and Supplementary Figure 3B**). Consistent with our previous
365 studies^{1,5,15-19,22}, all five histological parameters and the total histology score of
366 the Delta-infected hamsters were greatest (**Figure 6E**). On the other hand, these
367 scores were comparable in the three Omicron subvariant-infected hamsters
368 (**Figures 6D and 6E**).

369

370 **Impact of ORF9b:I5T on IFN-I inhibition and viral growth kinetics**

371 As shown in **Figure 1**, our epidemic dynamics analyses suggested that
372 ORF9b:I5T substitution contributes to the increased viral fitness in XBB lineages.
373 In addition to ORF9b:I5T, EG.5.1 has a substitution and a deletion in this protein
374 compared with Wuhan-Hu-1 (WH1)²⁷, both of which are conserved across
375 Omicron lineages (**Figure 7A**). Since previous studies demonstrated that
376 ORF9b inhibits IFN-I signaling⁷⁻¹⁰, we hypothesized that the I5T substitution
377 affects the anti-IFN-I function of ORF9b. To address this possibility, we used the
378 expression plasmid for the ORF9b protein of WH1²⁷ and compared its anti-IFN-I
379 activity with that of ORF6, another viral anti-IFN-I antagonist, which we showed
380 previously²⁸. As shown in **Figure 7B**, the anti-IFN-I activity of WH1 ORF9b was
381 less than that of WH1 ORF6. We then assessed the anti-IFN-I activity of ORF9b
382 of some SARS-CoV-2 Omicron subvariants such as XBB.1.5, XBB.1.16, and
383 EG.5.1. Although some values of Omicron subvariants were different from that
384 of WH1 with statistical significance, the anti-IFN-I activity was not clearly
385 different (**Figure 7C**). These findings suggest that the I5T substitution does not
386 critically affect the anti-IFN-I activity of ORF9b.

387 To further evaluate the impact of ORF9b:I5T on viral growth kinetics in
388 *in vitro* cell culture systems, we prepared three recombinant SARS-CoV-2,
389 rEG.5.1 [wildtype (WT)], rEG.5.1 ORF9b:T5I (ORF9b:T5I), and rEG.5.1 ORF9b
390 KO (ORF9b KO) by reverse genetics and inoculated it into multiple cell cultures.
391 As shown in **Figure 7D-H**, viral growth kinetics of ORF9b:T5I was comparable to
392 that of WT in all tested cell cultures, suggesting that the ORF9b:I5T does not
393 affect the viral replication efficacy. Similarly, the growth kinetics of WT and
394 ORF9b KO were comparable (**Figure 7D-H**). These findings suggest that

395 ORF9b does not have a crucial role on viral replication at least in *in vitro* cell
396 culture systems.

397 **Discussion**

398 In this study, we performed phylogenetic and epidemic dynamics modeling
399 analyses using viral sequence data and showed the data suggesting that two
400 hallmark mutations in the EG.5.1 lineage, S:F456L and ORF9b:I5T, are critical
401 to the increased viral fitness (i.e., R_e). We then experimentally addressed the
402 growth kinetics, sensitivity to clinically available antiviral compounds,
403 fusogenicity and pathogenicity of EG.5.1 and EG.5.1.1 variants. Our
404 experimental results suggest that the virological features of EG.5.1 and EG.5.1.1
405 are almost comparable to that of XBB.1.5. We further reveal the structure of
406 EG.5.1 S by cryo-EM and describe the structural difference between the EG.5.1
407 S and XBB.1.5 S. Moreover, we assessed the impact of ORF9b:I5T on the
408 function of IFN-I antagonism by ORF9b, while its impact was negligible at least
409 in our experimental setup. Furthermore, the experiments using the recombinant
410 EG.5.1 viruses by reverse genetics showed that the impact of ORF9b:I5T on
411 viral growth is not observed.

412

413 We have shown the evidence suggesting that the fusogenicity of S
414 protein in *in vitro* cell cultures (particularly in Calu-3 cells) is closely associated
415 with viral intrinsic pathogenicity in hamsters^{15,16,18}. Consistent with our
416 assumption, we demonstrated the fusogenicity of EG.5.1 S is comparable to that
417 of XBB.1.5 S (**Figure 4C**), and the infection experiment using airway-on-a-chip
418 showed that the potential of EG.5.1 to invade epithelial-endothelial barrier, which
419 reflects viral fusogenicity, is similar to that of XBB.1.5 (**Figures 4D and 4E**).
420 Moreover, in the experiments using hamsters, the intrinsic pathogenicity of
421 EG.5.1 is also indistinguishable to that of XBB.1.5 (**Figure 6**). Our results
422 suggest that the viral virulence is not modulated by the mutations accumulated in
423 the EG.5.1 genome when compared to XBB.1.5.

424

425 The ACE2 binding assay *in vitro* showed that the K_D value of EG.5.1 S
426 RBD is significantly higher than that of XBB.1.5 S RBD (**Figure 4A**). Consistent
427 with this observation, we have previously found that the pseudovirus infectivity of
428 EG.5.1 is also lower than that of XBB.1.5⁴. Additionally, the growth kinetics of
429 EG.5.1 does not outweigh that of XBB.1.5, while its extent is dependent on the
430 cell types used (**Figure 2**). Moreover, in hamsters, the spreading efficiency of
431 EG.5.1 is comparable to XBB.1.5 (**Figures 6B and 6C**). These observations
432 suggest that the growth capacity of EG.5.1 is similar to that of XBB.1.5. On the
433 other hand, as explained in the Introduction, recent studies including ours^{4,11}
434 showed that EG.5.1 exhibits significantly greater immune resistance to the
435 humoral immunity induced by XBB breakthrough infection than XBB.1.5, and the
436 S:F456L substitution is responsible for this immunological phenotype. Altogether,
437 these observations suggest that the epidemic spread of the EG.5.1 lineage by

438 outcompeting an S:F486P-bearing XBB subvariants including XBB.1.5, is not
439 due to increased viral growth capacity, but rather to increased immune evasion
440 capacity from the humoral immunity induced by XBB breakthrough infection.

441

442 The structure of EG.5.1 S alone revealed in this study provides an
443 opportunity to discuss the impact of the substitutions in S proteins occurring in
444 variants since BA.2.75 on a series of conformational changes from BA.2.75
445 through XBB.1 and XBB.1.5 to EG.5.1^{1,19,22}. It has been reported that the F486
446 residue stabilizes the 1-up state by hydrophobic interactions with the up RBD in
447 the 1-up conformation^{25,26}. In XBB.1 S, the 1-up conformation is not optimal due
448 to F486S substitution, a less bulky and hydrophilic residue. On the other hand,
449 XBB.1.5 and EG.5.1 S acquired commonly the F486P substitution, these
450 variants are thought to have the potential to stabilize an up RBD conformation,
451 but only EG.5.1 S was reconstructed in the 1-up conformation. This difference
452 between XBB.1.5 and EG.5.1 is probably related to the F456L substitution,
453 which resolved the interaction between protomers in closed 2 in EG.5.1 and
454 facilitated the transition from the closed state to the 1-up one. The amino-acid
455 substitution-dependent conformational transitions illuminated by this study
456 provide an understanding of metastable pre-fusions state of the spike protein in
457 omicron subvariant, BA.2.75, XBB.1, XBB.1.5 and EG.5.1.

458

459 **Limitation of the study**

460 Our epidemic dynamics modeling analysis suggests that S:F456L and
461 ORF9b:I5T enhance viral fitness in XBB lineages (**Figure. 1**). S:F456L likely
462 boosts viral fitness by improving the ability to escape humoral immunity induced
463 by vaccination and natural infection⁴. On the contrary, we failed to uncover any
464 notable effects of ORF9b:I5T on the viral properties we examined, including viral
465 replication in cell lines or airway organoids, or the inhibition of the IFN pathway
466 (**Figure. 7**). This discrepancy regarding the ORF9b:I5T might be attributed to
467 two potential explanations. First, the observed effect of ORF9b:I5T on viral
468 fitness could be a false positive. However, this seems less likely since the
469 positive effect of ORF9b:I5T on viral fitness was supported by two independent
470 methods: our approach and a method developed by Bloom et al., which infers
471 the fitness effect of a mutation based on its convergent acquisition level⁶. The
472 second explanation is that ORF9b:I5T might affect viral properties related to
473 fitness, which we did not investigate experimentally. Indeed, our understanding
474 of which properties of the virus are closely related to viral fitness is currently
475 limited. For a deeper understanding of the mechanism by which the virus boosts
476 its transmission potential, characterizing mutations in non-S proteins including
477 ORF9b:I5T would be crucial.

478

479 In sum, our multiscale investigation revealed the virological
480 characteristics of a most recently spreading SARS-CoV-2 variant, EG.5.1,
481 particularly focusing on the effects of hallmark substitutions in the S (F456L) and
482 non-S (ORF9b:I5T) proteins. As we demonstrated on a variety of SARS-CoV-2
483 Omicron subvariants in the past^{1,2,4,5,13,15,17-19,21,22,29-31}, elucidating the virological
484 features of newly emerging SARS-CoV-2 variants is important to consider the
485 potential risk to human society and to understand the evolutionary scenario of
486 the emerging virus in the human population. In particular, accumulating the
487 knowledge of the evolution trait of newly emerging pathogenic viruses in the
488 human population will be beneficial for future outbreak/pandemic preparedness.

489 **Author Contributions**

490 Sayaka Deguchi, MST Monira Begum, Hesham Nasser, Michael Jonathan,
491 Terumasa Ikeda, and Kazuo Takayama performed cell culture experiments.
492 Shuhei Tsujino and Tomokazu Tamura generated recombinant viruses.
493 Shuhei Tsujino, Keita Mizuma, Naganori Nao, Isshu Kojima, Tomoya Tsubo,
494 Jingshu Li, Kumiko Yoshimatsu, Rigel Suzuki, Tomokazu Tamura, Keita
495 Matsuno performed animal experiments.
496 Lei Wang, Yoshitaka Oda, Masumi Tsuda, Shinya Tanaka performed
497 histopathological analysis.
498 performed yeast surface display assay.
499 Sayaka Deguchi, Kazuo Takayama prepared human iPSC-derived lung
500 organoids, AO-ALI, and airway-on-a-chip systems.
501 Sayaka Deguchi, Kazuo Takayama performed antiviral drug tests
502 Yuki Yamamoto and Tetsuharu Nagamoto performed generation and provision
503 of human iPSC-derived airway and alveolar epithelial cells.
504 Hisano Yajima, Kaori Sasaki-Tabata and Takao Hashiguchi prepared the EG.5.1
505 S protein.
506 Tomo Nomai, Yuki Anraku, Shunsuke Kita, Katsumi Maenaka and Takao
507 Hashiguchi determined the structure of EG.5.1 S protein.
508 Hiroyuki Asakura, Mami Nagashima, Kenji Sadamasu and Kazuhisa Yoshimura
509 performed viral genome sequencing analysis.
510 Yasufumi Matsumura, Miki Nagao collected swab samples from COVID-19 and
511 performed viral genome sequencing analysis.
512 Arnon Plianchaisuk performed bioinformatics analyses.
513 Jumpei Ito designed bioinformatics analyses and interpreted the results.
514 Terumasa Ikeda, Takasuke Fukuhara, and Kei Sato designed the experiments
515 and interpreted the results.
516 Jumpei Ito, Terumasa Ikeda, Kazuo Takayama, Jiri Zahradnik, Takasuke
517 Fukuhara and Kei Sato wrote the original manuscript.
518 All authors reviewed and proofread the manuscript.
519 The Genotype to Phenotype Japan (G2P-Japan) Consortium contributed to the
520 project administration.

521

522 **Conflict of interest**

523 Yuki Yamamoto and Tetsuharu Nagamoto are founders and shareholders of
524 HiLung, Inc. Yuki Yamamoto is a co-inventor of patents (PCT/JP2016/057254;
525 "Method for inducing differentiation of alveolar epithelial cells",
526 PCT/JP2016/059786, "Method of producing airway epithelial cells"). Jumpei Ito
527 has consulting fees and honoraria for lectures from Takeda Pharmaceutical Co.
528 Ltd. Kei Sato has consulting fees from Moderna Japan Co., Ltd. and Takeda
529 Pharmaceutical Co. Ltd. and honoraria for lectures from Gilead Sciences, Inc.,

530 Moderna Japan Co., Ltd., and Shionogi & Co., Ltd. The other authors declare
531 that no competing interests exist.

532

533 **Acknowledgments**

534 We would like to thank all members belonging to The Genotype to Phenotype
535 Japan (G2P-Japan) Consortium. We thank Dr. Kenzo Tokunaga (National
536 Institute for Infectious Diseases, Japan) and Dr. Jin Gohda (The University of
537 Tokyo, Japan) for providing reagents. We thank to all members belonging to
538 Japanese Consortium on Structural Virology (JX-Vir). We appreciate the
539 technical assistance from The Research Support Center, Research Center for
540 Human Disease Modeling, Kyushu University Graduate School of Medical
541 Sciences. We gratefully acknowledge all data contributors, i.e. the Authors and
542 their Originating laboratories responsible for obtaining the specimens, and their
543 Submitting laboratories for generating the genetic sequence and metadata and
544 sharing via the GISAID Initiative, on which this research is based. The
545 super-computing resource was provided by Human Genome Center at The
546 University of Tokyo.

547 This study was supported in part by AMED SCARDA Japan Initiative
548 for World-leading Vaccine Research and Development Centers "UTOPIA"
549 (JP223fa627001, to Kei Sato), AMED SCARDA Program on R&D of new
550 generation vaccine including new modality application (JP223fa727002, to Kei
551 Sato); AMED SCARDA Kyoto University Immunomonitoring Center (KIC)
552 (JP223fa627009, to Takao Hashiguchi); AMED SCARDA Hokkaido University
553 Institute for Vaccine Research and Development (HU-IVReD) (JP223fa627005,
554 to Katsumi Maenaka); AMED Research Program on Emerging and Re-emerging
555 Infectious Diseases (JP21fk0108574, to Hesham Nasser; JP21fk0108493, to
556 Takasuke Fukuhara; JP22fk0108617 to Takasuke Fukuhara; JP22fk0108146, to
557 Kei Sato; JP21fk0108494 to G2P-Japan Consortium, Keita Matsuno, Shinya
558 Tanaka, Terumasa Ikeda, Takasuke Fukuhara, and Kei Sato; JP21fk0108425,
559 to Kazuo Takayama and Kei Sato; JP21fk0108432, to Kazuo Takayama,
560 Takasuke Fukuhara and Kei Sato; JP22fk0108534, to Takashi Irie, Terumasa
561 Ikeda, and Kei Sato; JP22fk0108511, to Yuki Yamamoto, Terumasa Ikeda, Keita
562 Matsuno, Shinya Tanaka, Kazuo Takayama, Takao Hashiguchi, Takasuke
563 Fukuhara, and Kei Sato); AMED Research Program on HIV/AIDS
564 (JP22fk0410055, to Terumasa Ikeda; and JP22fk0410039, to Kei Sato); AMED
565 Japan Program for Infectious Diseases Research and Infrastructure
566 (JP22wm0125008 to Keita Matsuno); AMED CREST (JP21gm1610005, to
567 Kazuo Takayama; JP22gm1610008, to Takasuke Fukuhara; JP22gm1810004,
568 to Katsumi Maenaka); JST PRESTO (JPMJPR22R1, to Jumpei Ito); JST CREST
569 (JPMJCR20H4, to Kei Sato; JPMJCR20H8, to Takao Hashiguchi); JSPS
570 KAKENHI Grant-in-Aid for Scientific Research C (22K07103, to Terumasa

571 Ikeda); JSPS KAKENHI Grant-in-Aid for Scientific Research B (21H02736, to
572 Takasuke Fukuhara); JSPS KAKENHI Grant-in-Aid for Early-Career Scientists
573 (22K16375, to Hesham Nasser; 20K15767, Jumpei Ito); JSPS KAKENHI grant
574 JP20H05873 (to Katsumi Maenaka); JSPS Core-to-Core Program (A. Advanced
575 Research Networks) (JPJSCCA20190008, to Kei Sato); JSPS Research Fellow
576 DC2 (22J11578, to Keiya Uriu); JSPS Leading Initiative for Excellent Young
577 Researchers (LEADER) (to Terumasa Ikeda); World-leading Innovative and
578 Smart Education (WISE) Program 1801 from the Ministry of Education, Culture,
579 Sports, Science and Technology (MEXT) (to Naganori Nao); Research Support
580 Project for Life Science and Drug Discovery [Basis for Supporting Innovative
581 Drug Discovery and Life Science Research (BINDS)] from AMED under the
582 Grant JP22ama121001 (to Takao Hashiguchi) and JP22ama121037 (to Katsumi
583 Maenaka); The Cooperative Research Program (Joint Usage/Research Center
584 program) of Institute for Life and Medical Sciences, Kyoto University (to Kei Sato
585 and Katsumi Maenaka); International Joint Research Project of the Institute of
586 Medical Science, the University of Tokyo (to Terumasa Ikeda, Jiri Zahradnik,
587 and Takasuke Fukuhara); The Tokyo Biochemical Research Foundation (to Kei
588 Sato); Takeda Science Foundation (to Terumasa Ikeda and Katsumi Maenaka);
589 Mochida Memorial Foundation for Medical and Pharmaceutical Research (to
590 Terumasa Ikeda); The Naito Foundation (to Terumasa Ikeda); Mitsubishi
591 Foundation (to Kei Sato); and the project of National Institute of Virology and
592 Bacteriology, Programme EXCELES, funded by the European Union, Next
593 Generation EU (LX22NPO5103, to Jiri Zahradnik).

594

595 **Consortia**

596 Hirofumi Sawa¹¹, Tomoya Tsubo¹¹, Zannatul Ferdous⁷, Kenji Shishido⁷, Saori
597 Suzuki¹, Hayato Ito¹, Yu Kaku⁶, Naoko Misawa⁶, Kaoru Usui⁶, Wilaiporn
598 Saikruang⁶, Yusuke Kosugi⁶, Shigeru Fujita⁶, Jarel Elgin M. Tolentino⁶, Luo
599 Chen⁶, Lin Pan⁶, Mai Suganami⁶, Mika Chiba⁶, Ryo Yoshimura⁶, Kyoko Yasuda⁶,
600 Keiko Iida⁶, Adam P. Strange⁶, Naomi Ohsumi⁶, Shiho Tanaka⁶, Kaho Okumura⁶,
601 Daniel Sauter^{6,36}, Isao Yoshida²⁰, So Nakagawa³⁶, Kotaro Shirakawa³⁷, Akifumi
602 Takaori-Kondo³⁷, Kayoko Nagata³⁷, Ryosuke Nomura³⁷, Yoshihito Horisawa³⁷,
603 Yusuke Tashiro³⁷, Yugo Kawai³⁷, Rina Hashimoto², Yukio Watanabe², Yoshitaka
604 Nakata², Hiroki Futatsusako², Ayaka Sakamoto², Naoko Yasuhara², Tateki
605 Suzuki¹⁶, Kanako Terakado Kimura¹⁶, Jiei Sasaki¹⁶, Yukari Nakajima¹⁶, Ryoko
606 Kawabata²⁹, Ryo Shimizu⁹, Yuka Mugita⁹, Sharee Leong⁹, Otowa Takahashi⁹,
607 Kimiko Ichihara⁹, Chihiro Motozono³⁸, Mako Toyoda³⁸, Takamasa Ueno³⁸,
608 Akatsuki Saito³⁹, Maya Shofa³⁹, Yuki Shibatani³⁹, Tomoko Nishiuchi³⁹,
609 Prokopios Andrikopoulos⁴, Aditi Konar⁴

610

611 ³⁶Tokai University School of Medicine, Isehara, Japan

- 612 ³⁷Kyoto University, Kyoto, Japan
613 ³⁸Kumamoto University, Kumamoto, Japan
614 ³⁹Miyazaki University, Miyazaki, Japan

615 **Figure legends**

616 **Figure 1. Mutations contributing to increased viral fitness of EG.5.1**

617 (A) Frequency of mutations in the EG.5, EG.5.1, EG.5.1.1, and other
618 representative XBB subvariants. Only mutations with a frequency >0.5 in at least
619 one but not all subvariants of interest are shown.

620 (B) A phylogenetic tree of SARS-CoV-2 in the XBB lineage. Only genomic
621 sequences of SARS-CoV-2 isolates in XBB, XBB.1, EG.5, and EG.5.1
622 subvariants are marked with tip labels. The ultrafast bootstrap value of the
623 common ancestor of XBB.1.9, XBB.1.16, and XBB.1.22 and that of the MRCA of
624 EG.5 are 28 and 100, respectively. The heatmap on the right represents the
625 presence or absence of ORF9b:I5T and S:F456L substitutions in each
626 SARS-CoV-2 isolate. A diamond symbol represents an inferred common
627 ancestor with an occurrence of ORF9b:I5T or S:F456L substitution. Only the
628 occurrence events of ORF9b:I5T and S:F456L substitutions at an internal node
629 having at least 10 descendant tips are shown. The scale bar denotes genetic
630 distance.

631 (C) Effect of substitutions in the 12 SARS-CoV-2 proteins on relative R_e . The
632 genome surveillance data for SARS-CoV-2 in XBB lineages circulated in the
633 USA from December 1, 2022 to September 15, 2023 was analyzed. The
634 posterior mean (dot) and 95% Bayesian confidential interval (CI; error bar) are
635 shown. A group of highly co-occurred substitutions was treated as a substitution
636 cluster. Substitutions specifically present in EG.5.1 or EG.5.1.1 compared with
637 XBB.1.5 are labeled.

638 (D) Relative R_e of SARS-CoV-2 haplotypes in the XBB lineage. The value for the
639 major haplotype of XBB.1.5 is set at 1. The posterior mean (dot) and 95%
640 Bayesian CI (error bar) are shown. The left heatmap represents the presence or
641 absence of the ORF9b:I5T and S:F456L substitutions in each haplotype.

642

643 **Figure 2. Growth kinetics of EG.5.1 and EG.5.1.1**

644 Clinical isolates of Delta, XBB.1.5, EG.5.1, and EG.5.1.1 were inoculated into
645 Vero cells (A), VeroE6/TMPRSS2 cells (B), 293-ACE2/TMPRSS2 cells (C),
646 Calu-3 cells (D), airway organoids-derived ALI model (E), and human
647 iPSC-derived lung alveolar cells (F). The copy numbers of viral RNA in the
648 culture supernatant (A–F) were routinely quantified by RT-qPCR.

649

650 **Figure 3. Effects of four antiviral drugs against EG.5.1 and EG.5.1.1 in**
651 **human iPSC-derived lung organoids**

652 Antiviral effects of the three drugs [Remdesivir, Ensitrelvir, and Nirmatrelvir (also
653 known as PF-07321332)] in human iPSC-derived lung organoids. The assay of
654 each antiviral drugs was performed in triplicate, and the 50% effective
655 concentration (EC_{50}) was calculated.

656

657 **Figure 4. Fusogenicity of EG.5.1**

658 **(A)** Binding affinity of the receptor binding domain (RBD) of SARS-CoV-2 spike
659 (S) protein to angiotensin- converting enzyme 2 (ACE2) by yeast surface display.
660 The dissociation constant (K_D) value indicating the binding affinity of the RBD of
661 the SARS-CoV-2 S protein to soluble ACE2 when expressed on yeast is shown.
662 The horizontal dashed line indicates value of XBB.1.5.
663 **(B)** Mean fluorescence intensity (MFI) of the surface S expression level in
664 HEK293 cells. **(C)** SARS-CoV-2 S protein-mediated membrane fusion assay in
665 Calu-3/DSP₁₋₇ cells. **(D, E)** Clinical isolates of Delta, XBB.1.5, EG.5.1, and
666 EG.5.1.1 were inoculated into an airway-on-a-chip system. The copy numbers of
667 viral RNA in the top and bottom channels of an airway-on-a-chip were routinely
668 quantified by RT-qPCR **(D)**. The percentage of viral RNA load in the bottom
669 channel per top channel at 6 d.p.i. (i.e., % invaded virus from the top channel to
670 the bottom channel) is shown **(E)**. Assays were performed in triplicate **(B, D, E)**
671 or quadruplicate **(C)**. The presented data are expressed as the average \pm
672 standard deviation (SD) **(B-E)**. For panel **C**, statistical differences between
673 XBB.1.5 S and each S variant across timepoints were determined by multiple
674 regression and *P* values are indicated in each graph. The 0 h data were
675 excluded from the analyses. The FWERs (Family-wise error rates) calculated
676 using the Holm method are indicated in the figures.

677

678 **Figure 5. Overall cryo-EM maps and structures of SARS-CoV-2 EG.5.1 S** 679 **protein**

680 **(A)** Cryo-EM maps of EG.5.1 S protein trimer closed-1 state **(Left)**, closed-2
681 state **(Middle)** and 1-up state **(Right)**. Each protomer is colored red, blue, gray.
682 **(B)** Superimposed structures of EG.5.1 (red) and XBB.1.5 (cyan) S protomers in
683 closed-2 state. The models were superposed on the C α atoms of the
684 corresponding residues in the S2 region (RMSD = 0.244).
685 **(C)** Close-up views of the amino-acid residues 456 and 373 in closed-2
686 structures. **(Left)** F456 at the protomer interface in the XBB.1.5 S RBD region
687 makes hydrophobic contact with P373 in adjacent protomer at a distance of 3.8
688 Å. **(Right)** F456L substitution causes loss of hydrophobic contact with P373, up
689 to 10.1 Å away.
690 **(D)**. Close-up view of the interface between up RBD and adjacent down
691 protomer. The model of EG.5.1 closed-2 RBD was rigid-fitted to the
692 corresponding region of the cryo-EM map of EG.5.1 S protein 1-up state.

693

694 **Figure 6. Virological characteristics of EG.5.1 and EG.5.1.1 *in vivo***

695 Syrian hamsters were intranasally inoculated with EG.5.1, EG.5.1.1, XBB.1.5,
696 and Delta. Six hamsters of the same age were intranasally inoculated with saline

697 (uninfected). Six hamsters per group were used to routinely measure the
698 respective parameters **(A)**. Four hamsters per group were euthanized at 2 and 5
699 d.p.i. and used for virological and pathological analysis **(C–E)**.

700 **(A)** Body weight, Penh, and Rpef values of infected hamsters ($n = 6$ per infection
701 group).

702 **(B)** **(Left)** Viral RNA loads in the oral swab ($n = 6$ per infection group). **(Middle**
703 **and right)** Viral RNA loads in the lung hilum **(middle)** and lung periphery **(right)**
704 of infected hamsters ($n = 4$ per infection group).

705 **(C)** IHC of the viral N protein in the lungs at 2 d.p.i. **(left)** and 5 d.p.i. **(right)** of
706 infected hamsters. Representative figures (N-positive cells are shown in brown).

707 **(D)** H&E staining of the lungs of infected hamsters. Representative figures are
708 shown in **(D)**. Uninfected lung alveolar space is also shown. The raw data are
709 shown in **Supplementary Figure 1**.

710 **(E)** Histopathological scoring of lung lesions ($n = 4$ per infection group).
711 Representative pathological features are reported in our previous
712 studies^{15-17,32-35}. In **A–C, E**, data are presented as the average \pm SEM. In **C**,
713 each dot indicates the result of an individual hamster.

714 In **A,B,E**, statistically significant differences between EG.5.1, EG.5.1.1 and other
715 variants across timepoints were determined by multiple regression. In **B,E**, the 0
716 d.p.i. data were excluded from the analyses. The FWERs calculated using the
717 Holm method are indicated in the figures.

718 In **C**, the statistically significant differences between EG.5.1, EG.5.1.1 and other
719 variants were determined by a two-sided Mann–Whitney U test.

720 In **C** and **D**, each panel shows a representative result from an individual infected
721 hamster. Scale bars, 200 μ m **(C, D)**.

722

723 **Figure 7. Impact of the I5T substitution of ORF9b on innate immune** 724 **response and viral growth**

725 **(A–C)** Anti-IFN-I effect of ORF9b:I5T.

726 **(A)** Frequency of mutations in ORF9b of BA.1, BA.2, XBB.1.5, XBB.1.16, and
727 EG.5.1. Only mutations with a frequency >0.5 in at least a subvariant are shown.

728 **(B)** Comparison of the anti-IFN-I effect and expression levels between ORF9b
729 and ORF6 in HEK293 cells. HEK293 cells were cotransfected with plasmids
730 expressing 2 \times Strep-tagged ORF9b or ORF6 and p125Luc. 24 h after
731 transfection, cells were infected with SeV (MOI 100). 24 h after infection, cells
732 were harvested for western blotting **(top)** and a luciferase assay **(bottom)**.

733 **(C)** Comparison of the anti-IFN-I effect and expression levels of ORF9b among
734 SARS-CoV-2 variants in HEK293 cells. HEK293 cells were cotransfected with
735 plasmids expressing 2 \times Strep-tagged ORF9b variants and p125Luc. 24 h after
736 transfection, cells were infected with SeV (MOI 100). 24 h after infection, cells
737 were harvested for western blotting **(top)** and a luciferase assay **(bottom)**. For

738 Western blotting (**B, top** and **C, top**), the input of cell lysate was normalized to
739 TUBA, and one representative result out of three independent experiments is
740 shown. kDa, kilodalton. For the luciferase assay (**B, bottom** and **C, bottom**), the
741 value was normalized to the unstimulated, empty vector-transfected cells (no
742 SeV infection).

743 (**D–H**) Three recombinant SARS-CoV-2, rEG.5.1 WT, rEG.5.1 ORF9b:T5I
744 (ORF9b:T5I), and rEG.5.1 ORF9b KO (ORF9b KO) were inoculated into Vero
745 cells (**D**), VeroE6/TMPRSS2 cells (**E**), 293-ACE2/TMPRSS2 cells (**F**), Calu-3
746 cells (**G**), and airway organoids-derived ALI model (**H**). The copy numbers of
747 viral RNA in the culture supernatant (**D–H**) were routinely quantified by
748 RT-qPCR. The dashed red line indicates the results of WT.

749 In **B**, the statistically significant differences between the stimulated, empty
750 vector-transfected cells (SeV infection) and the stimulated, ORF9b or ORF6
751 expression vector-transfected cells were determined by a two-sided Student's *t*
752 test.

753 In **C**, the statistically significant differences between the stimulated, ORF9b
754 expression vector-transfected cells and the stimulated, ORF6 expression
755 vector-transfected cells at the same dose respectively were determined by a
756 two-sided Student's *t* test.

757

758 **Supplementary files**

759 **Supplementary Table 1.** Effect of amino acid substitution in the 12
760 SARS-CoV-2 proteins on R_e and relating modeling parameters of SARS-CoV-2
761 in the XBB lineage circulated in the USA from December 1, 2022 to September
762 15, 2023.

763

764 **Supplementary Table 2.** Estimated relative R_e and modeling parameters of
765 haplotypes of SARS-CoV-2 in the XBB lineage circulated in the USA from
766 December 1, 2022 to September 15, 2023.

767

768 **Supplementary Table 3.** Cryo-EM data collection, refinement and validation
769 statistics

770

771 **Supplementary Table 4.** Primers used in this study for preparation of
772 SARS-CoV-2 ORF9b expression plasmid

773

774 **Supplementary Table 5.** Summary of unexpected amino acid mutations
775 detected in the working virus stocks

776

777 **Supplementary Figure 1. Workflow of cryo-EM data processing for EG.5.1**
778 **S and structural comparison for EG.5.1 and XBB.1.5 S, related to Figure 5**

779 **(A) (Left)** Representative micrograph (scale bars, 50 nm) and 2D class images.
780 **(Right)** Cryo-EM data processing flowchart for EG.5.1 S. **(B)** Global resolution
781 assessment of cryo-EM maps by gold-standard Fourier shell correlation (FSC)
782 curves at the 0.143 criteria. The calculated values of local resolution was colored
783 at grid point of cryo-EM maps. **(C)** Superimposed RBD structures of EG.5.1 S
784 closed-1 and closed-2. An arrow indicates 370-375 residues of RBD that show
785 different loop structure in these two closed states. **(D)** Superimposed amino-acid
786 residues that are substituted in closed-1 state of spike protein in EG.5.1 (red) as
787 compared to XBB.1.5 (cyan). **(E)** The models fit to corresponding cryo-EM
788 maps at Q52H and F456L substitution. Arrows indicate the substituted
789 amino-acid residues, Q52H and F456L, between EG.5.1 and XBB.1.5.

790

791 **Supplementary Figure 2. Distribution of SARS-CoV-2 N-positive cells in the**
792 **lungs of infected hamsters, related to Figure 6**

793 N-positive area in the lungs of infected hamsters at 2 d.p.i **(A)** and 5 d.p.i **(B)** (4
794 hamsters per infection group). N-protein immunohistochemistry(top) and the
795 digitalized N-positive area (bottom, indicated in red) are shown. The red
796 numbers in the bottom panels indicate the percentage of N-positive area.
797 Summarized data are shown in a bar graph (right). Representative images are
798 shown in **Figure 6C**.

799

800 **Supplementary Figure 3. Histological observations in infected hamsters,**
801 **related to Figure 6**

802 Type II pneumocytes in the lungs of infected hamsters at 2 d.p.i. **(A)** and 5 d.p.i
803 **(B)** (4 hamsters per infection group). H&E staining (top) and the digitalized
804 inflammatory area with type II pneumocytes (bottom, indicated in red) are shown.
805 The red numbers in the bottom panels indicate the percentage of inflammatory
806 area with type II pneumocytes. Summarized data are shown in a bar graph
807 **(right)**. Representative images are shown in **Figure 6D**.

808

809 **Figure S4. Protein-engineered mACE2 protein, related to Figure 4**

810 **(A)** mACE2 protein isolated after one purification step on-column cleavage by
811 bdSUMO-protease. Molecular size marker is Flash Protein Ladder, FPL-008,
812 Gel Company, USA.

813 **(B)** Comparison between mACE2 and Expi293F cells produced ACE2 peptidase
814 domain shows tighter interactions with the mACE2 despite the intact binding site.
815 Notably, the effect of mutations in different RBDs is similar between ACE2-WT
816 and mACE2.

817 **Methods**

818

819 **Ethics statement**

820 All experiments with hamsters were performed in accordance with the Science
821 Council of Japan's Guidelines for the Proper Conduct of Animal Experiments.
822 The protocols were approved by the Institutional Animal Care and Use
823 Committee of National University Corporation Hokkaido University (approval ID:
824 20-0123 and 20-0060). All protocols involving specimens from human subjects
825 recruited at Kyoto University. All human subjects provided written informed
826 consent. All protocols for the use of human specimens were reviewed and
827 approved by the Institutional Review Board of Kyoto University (approval ID:
828 R2379-3).

829

830 **Cell culture**

831 HEK293T cells (a human embryonic kidney cell line; ATCC, CRL-3216),
832 HEK293 cells (a human embryonic kidney cell line; ATCC, CRL-1573) and
833 HOS-ACE2/TMPRSS2 cells (HOS cells stably expressing human ACE2 and
834 TMPRSS2)^{36,37} were maintained in DMEM (high glucose) (Sigma-Aldrich, Cat#
835 6429-500ML) containing 10% fetal bovine serum (FBS, Sigma-Aldrich Cat#
836 172012-500ML) and 1% penicillin–streptomycin (PS) (Sigma-Aldrich, Cat#
837 P4333-100ML). HEK293-ACE2 cells (HEK293 cells stably expressing human
838 ACE2)¹⁴ were maintained in DMEM (high glucose) containing 10% FBS, 1 µg/ml
839 puromycin (InvivoGen, Cat# ant-pr-1) and 1% PS. HEK293-ACE2/TMPRSS2
840 cells (HEK293 cells stably expressing human ACE2 and TMPRSS2)¹⁴ were
841 maintained in DMEM (high glucose) containing 10% FBS, 1 µg/ml puromycin,
842 200 µg/ml hygromycin (Nacalai Tesque, Cat# 09287-84) and 1% PS. Vero cells
843 [an African green monkey (*Chlorocebus sabaeus*) kidney cell line; JCRB Cell
844 Bank, JCRB0111] were maintained in Eagle's minimum essential medium
845 (EMEM) (Sigma-Aldrich, Cat# M4655-500ML) containing 10% FBS and 1% PS.
846 VeroE6/TMPRSS2 cells (VeroE6 cells stably expressing human TMPRSS2;
847 JCRB Cell Bank, JCRB1819)³⁸ were maintained in DMEM (low glucose) (Wako,
848 Cat# 041-29775) containing 10% FBS, G418 (1 mg/ml; Nacalai Tesque, Cat#
849 G8168-10ML) and 1% PS. Calu-3 cells (ATCC, HTB-55) were maintained in
850 Eagle's minimum essential medium (EMEM) (Sigma-Aldrich, Cat#
851 M4655-500ML) containing 10% FBS and 1% PS. Calu-3/DSP₁₋₇ cells (Calu-3
852 cells stably expressing DSP₁₋₇)³⁹ were maintained in EMEM (Wako, Cat#
853 056-08385) containing 20% FBS and 1% PS. Human alveolar epithelial cells
854 derived from human induced pluripotent stem cells (iPSCs) were manufactured
855 according to established protocols as described below (see "Preparation of
856 human alveolar epithelial cells from human iPSCs" section) and provided by
857 HiLung Inc. AO-ALI model was generated according to established protocols as

858 described below (see “AO-ALI model” section). Human iPSC-derived lung
859 organoids were generated according to established protocols as described
860 below (see “iPSC-derived lung organoids” section). Expi293F cells (Thermo
861 Fisher Scientific, Cat# A14527) were maintained in Expi293 expression medium
862 (Thermo Fisher Scientific, Cat# A1435101).

863

864 **Viral genome sequencing**

865 Viral genome sequencing was performed as previously described¹⁸. Briefly, the
866 virus sequences were verified by viral RNA-sequencing analysis. Viral RNA was
867 extracted using a QIAamp viral RNA mini kit (Qiagen, Cat# 52906). The
868 sequencing library employed for total RNA sequencing was prepared using the
869 NEBNext Ultra RNA Library Prep Kit for Illumina (New England Biolabs, Cat#
870 E7530). Paired-end 76-bp sequencing was performed using a MiSeq system
871 (Illumina) with MiSeq reagent kit v3 (Illumina, Cat# MS-102-3001). Sequencing
872 reads were trimmed using fastp v0.21.0⁴⁰ and subsequently mapped to the viral
873 genome sequences of a lineage B isolate (strain Wuhan-Hu-1; GenBank
874 accession number: NC_045512.2)³⁸ using BWA-MEM v0.7.17⁴¹. Variant calling,
875 filtering, and annotation were performed using SAMtools v1.9⁴² and snpEff
876 v5.0e⁴³.

877

878 **Mutation frequency calculation and phylogenetic tree reconstruction**

879 Genomic sequences and surveillance data of 15,886,795 SARS-CoV-2 isolates
880 were obtained from the GISAID database on August 21, 2023
881 (<https://www.gisaid.org>)⁴⁴. The PANGO lineage of each isolate was reassigned
882 using NextClade v2.14.0⁴⁵. We excluded the data of SARS-CoV-2 isolate that i)
883 was collected after August 15, 2023; ii) was isolated from non-human hosts; iii)
884 was sampled from the original passage; and iv) whose genomic sequence is not
885 longer than 28,000 base pairs and contains $\geq 2\%$ of unknown (N) nucleotides.

886 We randomly selected at most 500 genomic sequences of
887 SARS-CoV-2 in BA.1, BA.2, XBB, XBB.1, XBB.1.5, XBB.1.9, XBB.1.9.2, EG.5,
888 EG.5.1, and EG.5.1.1 for calculating a mutation frequency (EPI SET ID:
889 EPI_SET_231018pe). A mutation frequency of each subvariant is calculated by
890 dividing the number of sequences harboring the substitution of interest with the
891 total number of sequences in that subvariant.

892 Next, we randomly selected at most 20 genomic sequences of
893 SARS-CoV-2 in each XBB subvariant, resulting in 4,906 genomic sequences of
894 SARS-CoV-2 from 248 XBB subvariants (EPI SET ID: EPI_SET_231003ue) to
895 reconstruct a phylogenetic tree of SARS-CoV-2 in the XBB lineage. The
896 sampled genomic sequences were aligned to the genomic sequence of
897 Wuhan-Hu-1 SARS-CoV-2 isolate (NC_045512.2) using reference-guide
898 multiple pairwise alignment strategy implemented in ViralMSA v1.1.24⁴⁶. Gaps in

899 the alignment were removed automatically using TrimAl v1.4.rev22 with
900 -gappyout mode⁴⁷, and the flanking edges of the alignment at positions 1–341
901 and 29,557–29,624 were trimmed manually. A maximum likelihood-based
902 phylogenetic tree of representative XBB sublineages was then reconstructed
903 from the alignment using IQ-TREE v2.2.0⁴⁸. The best-fit nucleotide substitution
904 model was selected automatically using ModelFinder⁴⁹. Branch support was
905 assessed using ultrafast bootstrap approximation⁵⁰ with 1,000 bootstrap
906 replicates. We omitted a genomic sequence of Wuhan-Hu-1 from the
907 reconstructed tree and manually rooted the tree using the MRCA node including
908 SARS-CoV-2 isolates in the original XBB subvariant.

909

910 **Reconstruction of the ancestral state of mutation**

911 The state of having or lacking ORF9b:I5T and S:F456L substitutions was
912 assigned to terminal nodes of the reconstructed tree based on the mutation
913 calling data from the GISAID database. We then reconstructed the state of
914 having ORF9b:I5T and S:F456L substitutions in the ancestral nodes from the
915 mutation calling data obtained from the GISAID database. The reconstruction
916 was performed using ace function of the ape R package v.5.7-1⁵¹ with equal-rate
917 model. The ancestral node with a scaled likelihood of having the mutation at
918 least 0.5 is considered having the mutation, whereas the ancestral node with the
919 scaled likelihood less than 0.5 is considered lacking the mutation. The
920 occurrence event of ORF9b:I5T and S:F456L substitutions was determined from
921 the state change from lacking mutation in the ancestral node to having mutation
922 in the adjacent descendant node. The reconstructed tree was visualized using
923 the ggtree R package v3.8.2⁵². All the phylogenetic analyses were aided by R
924 v4.3.1⁵³.

925

926 **Modeling the relationship between amino acid substitutions and epidemic 927 dynamics**

928 We modeled the relationship between amino acid substitutions (not including
929 deletions and insertions) and epidemic dynamics of SARS-CoV-2 in the XBB
930 lineage collected in the USA from December 1, 2022 to August 15, 2023 (EPI
931 SET ID: EPI_SET_231003vx). We used the Bayesian hierarchical multinomial
932 logistic model described in detail in our previous study⁵. Briefly, the
933 SARS-CoV-2 isolates were categorized into haplotypes based on their
934 substitution profile. Substitutions observed in >200 isolates but <90% of the total
935 isolates were selected to create the substitution profile matrix. The haplotype
936 with <30 isolates were excluded. We also identified a cluster of co-occurring
937 substitutions by connecting a substitution pair having Pearson's correlation >0.9,
938 resulting in profiles of 283 substitution clusters in 470 SARS-CoV-2 haplotypes.
939 The representative subvariant of each haplotype was identified using the

940 majority rule. We used an XBB.1.5 haplotype, the most abundant haplotype in
941 the dataset, as a reference for the modeling. Finally, we counted the number of
942 each haplotype collected in each day and created a count matrix.

943 Next, we applied our Bayesian hierarchical multinomial logistic model
944 to reconstruct the relationship between amino acid substitutions and epidemic
945 dynamics using the prepared substitution profile and count matrices. The model
946 is $y_{ht} \sim \text{Multinomial}(\sum_h y_{ht}, \text{softmax}(\alpha + \beta t))$ where y_{ht} is the count of
947 haplotype h at time t , α_h and β_h are intercept and slope (or growth rate)
948 parameters for haplotype h , respectively. The slope parameter β_h is derived
949 from the Student's t distribution Student's $t(\sum_m f_m X_{hm}, \sigma)$ with five degrees of
950 freedom where f_m is the effect of substitution cluster m , X_{hm} is the
951 substitution cluster profile of haplotype h , and σ is a standard deviation. We
952 used the Laplace distribution and half Student's t distribution with five degrees of
953 freedom as priors for f_m and σ , respectively. The mean and standard deviation
954 for both distributions were set to 0 and 10, respectively. Non-informative prior
955 was set for other parameters.

956 The relative R_e of each haplotype compared to the reference haplotype
957 or r_h is estimated from the equation $r_h = \exp(\gamma \beta_h)$ where β_h is the slope
958 parameter and γ is the average viral generation time (2.1 days)
959 ([http://sonorouschocolate.com/covid19/index.php?title=Estimating_Generation_](http://sonorouschocolate.com/covid19/index.php?title=Estimating_Generation_Time_Of_Omicron)
960 [Time_Of_Omicron](http://sonorouschocolate.com/covid19/index.php?title=Estimating_Generation_Time_Of_Omicron)). Similarly, the effect of each substitution on the relative R_e or
961 F_h is calculated according to the coefficient f_h using the equation $F_h =$
962 $\exp(\gamma f_h)$. Parameter estimation was performed by using the Markov chain
963 Monte Carlo (MCMC) approach implemented in CmdStan v2.31.0
964 (<https://mc-stan.org>) accessed through the CmdStanr v0.5.3 R interface
965 (<https://mc-stan.org/cmdstanr/>). Four independent 20,000-step MCMC chains
966 were run including 20% of warmup iterations. We confirmed that all runs have an
967 estimated convergence diagnostic value \hat{R} is <1.01 and bulk and tail effective
968 sampling sizes are >200 , indicating the successful convergence of each run.

969

970 **Plasmid construction**

971 Plasmids expressing the codon-optimized SARS-CoV-2 S proteins of B.1.1 (the
972 parental D614G-bearing variant), Delta, BA.2, XBB.1, XBB.1.5, EG.5 and the
973 two EG.5.1 derivatives were prepared in our previous studies^{1,2,4,14,16,17}.

974 Original human ACE2 protein (residues 19–615; GenBank Accession
975 Number NP_001358344.1) was modified to allow its efficient expression in
976 bacteria (*Escherichia coli* strain BL21), but residues participating in the
977 interaction with the SARS-CoV-2 RBD (5 Å distance) remained unaltered to
978 keep the interaction surface identical (details about the sequence of this
979 modified ACE2 protein are subjected to a separate publication and are available
980 upon request; hereinafter modified ACE2 protein will be referred as mACE2).

981 The mACE2 was inserted in pET28-14his-bdSUMO vector⁵⁴ by restriction-free
982 cloning and verified by sequencing.

983 Mammalian cell codon-optimized SARS-CoV-2 S RBDs of XBB.1 and
984 XBB.1.5 were amplified from the expression plasmids for the codon-optimized
985 SARS-CoV-2 S proteins of XBB.1¹ and XBB.1.5². The S RBDs of XBB.1.16 and
986 EG.5.1 were constructed by site-directed mutagenesis with primers:
987 XBB-K478R_R, 5'-CAG TTG GGG CCG GCC ACT CCA TTA CAT GGC CTG
988 TTG CCA GCC TGG TAA ATC TCT G-3' and XBB-F456L_R, 5'-GTC CCT CTC
989 AAA TGG TTT CAG CTT GCT CTT CCT CAA CAG TCT GTA GAG GTA GTT
990 GTA GTT GC-3'. All PCR reactions were performed by KAPA HiFi HotStart
991 ReadyMix kit (Roche, Cat# KK2601) and subsequently assembled by yeast
992 [*Saccharomyces cerevisiae* strain EBY100 (ATCC, Cat# MYA-4941)]
993 homologous recombination with pJYDC1 plasmid (Addgene, Cat# 162458) as
994 previously described^{1,5,18,19,55}.

995 Plasmids expressing the codon-optimized SARS-CoV-2 ORF9b and
996 ORF6 proteins were prepared in previous study (PMID: 32353859) (kindly
997 provided by Dr. Nevan J. Krogan). SARS-CoV-2 ORF9b-based derivatives were
998 generated by site-directed overlap extension PCR using the primers listed in
999 **Supplementary Table S4**. The resulting PCR fragment was digested with
1000 EcoRI (New England Biolabs, Cat# R3101S) and BamHI (New England Biolabs,
1001 Cat# R3136S) and inserted into the corresponding site of the
1002 pLVX-EF1alpha-IRES-Puro vector (PMID: 32353859). Nucleotide sequences
1003 were determined by DNA sequencing services (Eurofins), and the sequence
1004 data were analyzed by Sequencher v5.1 software (Gene Codes Corporation). To
1005 generate recombinant SARS-CoV-2, the nine pmW118 plasmid vectors were
1006 subjected to amplification of the cDNA fragments (F1-F9-10) of SARS-CoV-2
1007 EG.5.1. Nucleotide sequences were confirmed by a SeqStudio Genetic Analyzer
1008 (Thermo Fisher Scientific) and a DNA sequencing service (Fasmac).

1009

1010 **SARS-CoV-2 reverse genetics**

1011 Recombinant SARS-CoV-2 was generated by circular polymerase extension
1012 reaction (CPER) as previously described with modification^{14,17,31,56}. In brief, 9
1013 DNA fragments encoding the partial genome of SARS-CoV-2 were prepared by
1014 PCR using Q5 High-Fidelity DNA Polymerase (New England Biolabs, Cat#
1015 M0491S). A linker fragment encoding hepatitis delta virus ribozyme, bovine
1016 growth hormone poly A signal and cytomegalovirus promoter was also prepared
1017 by PCR with the primer-set described previously⁵⁶. The 10 obtained DNA
1018 fragments were mixed and used for CPER.

1019 To generate rEG.5.1-ORF9b KO and rEG.5.1-ORF9b:T5I (**Figure 7**),
1020 mutations were inserted in fragment 9 by inverse PCR-based site-directed

1021 mutagenesis with the primers listed in **Supplementary Table 4**. Nucleotide
1022 sequences were confirmed by the Sanger method as described above.

1023 To produce recombinant SARS-CoV-2, the CPER products (25 μ l)
1024 were transfected into VeroE6/TMPRSS2 cells using TransIT-X2 Dynamic
1025 Delivery System (Takara, Cat# MIR6003) according to our previous report²². The
1026 working virus stock was prepared from the seed virus as described below (see
1027 “SARS-CoV-2 preparation and titration” section below).

1028

1029 **SARS-CoV-2 preparation and titration**

1030 The working virus stocks of SARS-CoV-2 were prepared and titrated as
1031 previously described^{14,17,18,57}. In this study, clinical isolates of Delta (B.1.617.2,
1032 strain TKYTK1734; GISAID ID: EPI_ISL_2378732)¹⁶, XBB.1.5 (strain
1033 TKYmbc30523/2022; GISAID ID: EPI_ISL_16697941)²², EG.5.1 (strain
1034 KU2023071028; GISAID ID: EPI_ISL_18072016), and EG.5.1.1 (strain
1035 KU2023071635; GISAID ID: EPI_ISL_18072017) were used. Also, the artificially
1036 generated recombinant viruses by the CPER technique⁵⁶, rEG.5.1 WT, rEG.5.1
1037 ORF9b KO, rEG.5.1 ORF9b:T5I, were used. In brief, 20 μ l of the seed virus was
1038 inoculated into VeroE6/TMPRSS2 cells (5,000,000 cells in a T-75 flask). One
1039 h.p.i., the culture medium was replaced with DMEM (low glucose) (Wako, Cat#
1040 041-29775) containing 2% FBS and 1% PS. At 3 d.p.i., the culture medium was
1041 harvested and centrifuged, and the supernatants were collected as the working
1042 virus stock.

1043 The titer of the prepared working virus was measured as the 50%
1044 tissue culture infectious dose (TCID₅₀). Briefly, one day before infection,
1045 VeroE6/TMPRSS2 cells (10,000 cells) were seeded into a 96-well plate. Serially
1046 diluted virus stocks were inoculated into the cells and incubated at 37°C for 4 d.
1047 The cells were observed under a microscope to judge the CPE appearance. The
1048 value of TCID₅₀/ml was calculated with the Reed–Muench method⁵⁸.

1049 For verification of the sequences of SARS-CoV-2 working viruses, viral
1050 RNA was extracted from the working viruses using a QIAamp viral RNA mini kit
1051 (Qiagen, Cat# 52906) and viral genome sequences were analyzed as described
1052 above (see “Viral genome sequencing” section). Information on the unexpected
1053 substitutions detected is summarized in **Supplementary Table S5** and the raw
1054 data are deposited in the GitHub repository
1055 (<https://github.com/TheSatoLab/EG.5.1>).

1056

1057 **Yeast surface display**

1058 Yeast surface display analysis of the interaction between selected RBD variants
1059 and mACE2 (**Figure 4A**) was performed as previously described^{7,8,10,16,19,34,36,40}
1060 with some modification.

1061 The expression of mACE2 was initiated in 800 mL of 2YT autoinducible
1062 media with trace elements (ForMedium, Cat# AIM2YT0210) until optical density
1063 achieved 0.6 cultivated at 37°C. Subsequently, expression was further induced
1064 by the addition of IPTG to 0.25 mM and continued overnight, 20°C, 220 rpm. The
1065 bacteria culture was centrifuged (5 m, 4°C, 8,000 × g) and the pellet was
1066 resuspended in 15 ml of a loading buffer containing 50 mM Tris-HCl (pH 8.0) and
1067 200 mM NaCl. Cells were sonicated to extract the fused protein, centrifuged (10
1068 m, 4°C, 3,200 × g) and attached on the Ni-NTA column (2 ml). The column was
1069 washed by 10 CVs of the loading buffer supplemented with 10 mM imidazole
1070 and 10 CV of PBS. 50 µg of bdSUMO protease and 1 CV of PBS were loaded
1071 into the column for the proteolysis reaction (overnight at 4°C). Finally, the
1072 column was washed with 4 CV of PBS to obtain the cleaved mACE2, given that
1073 bdSUMO protease remained attached to the Ni-column thanks to the 14 ×
1074 His-tag it contained. This was proved after the elution with 4 CV of loading buffer
1075 supplemented with 300 mM imidazole and the subsequent analysis of all the
1076 loading, washing, and elution fractions by SDS-PAGE. Pure protein
1077 (**Supplementary Figure 4A**) was flash-frozen in liquid nitrogen and stored at
1078 -80°C.

1079 Yeast expression of SARS-CoV-2 S RBD was carried out for 48 h at
1080 20°C, and then cells were washed with PBS supplemented with bovine serum
1081 albumin at 1 g/l and incubated with 12 concentrations of mACE2 (4 pM to 10 nM,
1082 dilution series with factor 2) and 20 nM bilirubin (Sigma-Aldrich, Cat# 14370-1G).
1083 Performance comparison with Expi293F cells produced ACE2 peptidase domain
1084 (residues 18–617) was performed and is shown for XBB, XBB.1.5. and
1085 XBB.1.16. in **Supplementary Figure 4B**. RBD expression and ACE2 signal
1086 were recorded by using an automated acquisition from 96 well plates by
1087 CytoFLEX Flow Cytometer (Beckman Coulter), background binding signals were
1088 subtracted, fluorescence spill of eUnaG2 signals to red channel was
1089 compensated and data were fitted to a standard noncooperative Hill equation by
1090 nonlinear least-squares regression using Python v3.7 (<https://www.python.org>)
1091 as previously described^{7,8,10,16,19,34,36,40}.

1092

1093 **SARS-CoV-2 S-based fusion assay**

1094 A SARS-CoV-2 S-based fusion assay (**Figures 4B and 4C**) was performed as
1095 previously described^{1,5,14-21}. Briefly, on day 1, effector cells (i.e., S-expressing
1096 cells) and target cells (Calu-3/DSP₁₋₇ cells) were prepared at a density of 0.6–0.8
1097 × 10⁶ cells in a 6-well plate. On day 2, for the preparation of effector cells,
1098 HEK293 cells were cotransfected with the S expression plasmids (400 ng) and
1099 pDSP₈₋₁₁ (ref.⁵⁹) (400 ng) using TransIT-LT1 (Takara, Cat# MIR2300). On day 3
1100 (24 h posttransfection), 16,000 effector cells were detached and reseeded into a
1101 96-well black plate (PerkinElmer, Cat# 6005225), and target cells were reseeded

1102 at a density of 1,000,000 cells/2 ml/well in 6-well plates. On day 4 (48 h
1103 posttransfection), target cells were incubated with EnduRen live cell substrate
1104 (Promega, Cat# E6481) for 3 h and then detached, and 32,000 target cells were
1105 added to a 96-well plate with effector cells. *Renilla* luciferase activity was
1106 measured at the indicated time points using Centro XS3 LB960 (Berthold
1107 Technologies). For measurement of the surface expression level of the S protein,
1108 effector cells were stained with rabbit anti-SARS-CoV-2 S S1/S2 polyclonal
1109 antibody (Thermo Fisher Scientific, Cat# PA5-112048, 1:100). Normal rabbit IgG
1110 (Southern Biotech, Cat# 0111-01, 1:100) was used as a negative control, and
1111 APC-conjugated goat anti-rabbit IgG polyclonal antibody (Jackson
1112 ImmunoResearch, Cat# 111-136-144, 1:50) was used as a secondary antibody.
1113 The surface expression level of S proteins (**Figure 4B**) was measured using
1114 CytoFLEX Flow Cytometer (Beckman Coulter) and the data were analyzed using
1115 FlowJo software v10.7.1 (BD Biosciences). For calculation of fusion activity,
1116 *Renilla* luciferase activity was normalized to the mean fluorescence intensity
1117 (MFI) of surface S proteins. The normalized value (i.e., *Renilla* luciferase activity
1118 per the surface S MFI) is shown as fusion activity.

1119

1120 **AO-ALI model**

1121 An airway organoid (AO) model was generated according to our previous
1122 report^{19,60}. Briefly, normal human bronchial epithelial cells (NHBEs, Cat#
1123 CC-2540, Lonza) were used to generate AOs. NHBEs were suspended in 10
1124 mg/ml cold Matrigel growth factor reduced basement membrane matrix (Corning,
1125 Cat# 354230). Fifty microliters of cell suspension were solidified on prewarmed
1126 cell culture-treated multiple dishes (24-well plates; Thermo Fisher Scientific,
1127 Cat# 142475) at 37°C for 10 m, and then, 500 µl of expansion medium was
1128 added to each well. AOs were cultured with AO expansion medium for 10 d. For
1129 maturation of the AOs, expanded AOs were cultured with AO differentiation
1130 medium for 5 d.

1131 The AO-derived ALI (AO-ALI) model (**Figure 2E**) was generated
1132 according to our previous report^{19,60}. For generation of AO-ALI, expanding AOs
1133 were dissociated into single cells, and then were seeded into Transwell inserts
1134 (Corning, Cat# 3413) in a 24-well plate. AO-ALI was cultured with AO
1135 differentiation medium for 5 d to promote their maturation. AO-ALI was infected
1136 with SARS-CoV-2 from the apical side.

1137

1138 **Preparation of human iPSC-derived alveolar epithelial cells**

1139 The ALI culture of alveolar epithelial cells (**Figure 2F**) was differentiated from
1140 human iPSC-derived lung progenitor cells as previously described^{18,19,61-64}.
1141 Briefly, alveolar progenitor cells were induced stepwise from human iPSCs
1142 according to a 21-day and 4-step protocol⁶¹. At day 21, alveolar progenitor cells

1143 were isolated with the specific surface antigen carboxypeptidase M and seeded
1144 onto the upper chamber of a 24-well Cell Culture Insert (Falcon, #353104),
1145 followed by 7-day differentiation of alveolar epithelial cells. Alveolar
1146 differentiation medium with dexamethasone (Sigma-Aldrich, Cat# D4902), KGF
1147 (PeproTech, Cat# 100-19), 8-Br-cAMP (Biolog, Cat# B007), 3-isobutyl
1148 1-methylxanthine (IBMX) (Fujifilm Wako, Cat# 095-03413), CHIR99021 (Axon
1149 Medchem, Cat# 1386), and SB431542 (Fujifilm Wako, Cat# 198-16543) was
1150 used for the induction of alveolar epithelial cells.

1151

1152 **Preparation of human iPSC-derived lung organoids**

1153 Human iPSC-derived lung organoids were used for evaluation of antiviral drugs.
1154 The iPSC line (1383D6) (provided by Dr. Masato Nakagawa, Kyoto University)
1155 was maintained on 0.5 µg/cm² recombinant human laminin 511 E8 fragments
1156 (iMatrix-511 silk, Nippi, Cat# 892021) with StemFit AK02N medium (Ajinomoto,
1157 Cat# RCAF02N) containing 10 µM Y-27632 (FUJIFILM Wako Pure Chemical,
1158 Cat# 034-24024). For passaging, iPSC colonies were treated with TrypLE Select
1159 Enzyme (Thermo Fisher Scientific, Cat# 12563029) for 10 m at 37°C. After
1160 centrifugation, the cells were seeded onto Matrigel Growth Factor Reduced
1161 Basement Membrane (Corning, Cat# 354230)-coated cell culture plates (2.0 ×
1162 10⁵ cells/4 cm²) and cultured for 2 d. Lung organoids differentiation was
1163 performed in serum-free differentiation (SFD) medium of DMEM/F12 (3:1)
1164 (Thermo Fisher Scientific, Cat# 11320033) supplemented with N2 (FUJIFILM
1165 Wako Pure Chemical, Cat# 141-08941), B-27 Supplement Minus Vitamin A
1166 (Thermo Fisher Scientific, Cat# 12587001), ascorbic acid (50 µg/ml, STEMCELL
1167 Technologies, Cat# ST-72132), 1 × GlutaMAX (Thermo Fisher Scientific, Cat#
1168 35050-079), 1% monothioglycerol (FUJIFILM Wako Pure Chemical, Cat#
1169 195-15791), 0.05% bovine serum albumin, and 1 × PS. For definitive endoderm
1170 induction, the cells were cultured for 3 d (days 0–3) using SFD medium
1171 supplemented with 10 µM Y-27632 and 100 ng/mL recombinant Activin A (R&D
1172 Systems, Cat# 338-AC-010). For anterior foregut endoderm induction (days
1173 3–5), the cells were cultured in SFD medium supplemented with 1.5 µM
1174 dorsomorphin dihydrochloride (FUJIFILM Wako Pure Chemical, Cat#
1175 047-33763) and 10 µM SB431542 (FUJIFILM Wako Pure Chemical, Cat#
1176 037-24293) for 24 h and then in SFD medium supplemented with 10 µM
1177 SB431542 and 1 µM IWP2 (REPROCELL) for another 24 h. For the induction of
1178 lung progenitors (days 5–12), the resulting anterior foregut endoderm was
1179 cultured with SFD medium supplemented with 3 µM CHIR99021 (FUJIFILM
1180 Wako Pure Chemical, Cat# 032-23104), 10 ng/ml human FGF10 (PeproTech,
1181 Cat# 100-26), 10 ng/ml human FGF7 (PeproTech, Cat# 100-19), 10 ng/ml
1182 human BMP4 (PeproTech, Cat# 120-05ET), 20 ng/ml human EGF (PeproTech,
1183 Cat# AF-100-15), and all-trans retinoic acid (ATRA, Sigma-Aldrich, Cat# R2625)

1184 for 7 d. At 12 d of differentiation, the cells were dissociated and embedded in
1185 Matrigel Growth Factor Reduced Basement Membrane to generate organoids.
1186 For lung organoid maturation (days 12–30), the cells were cultured in SFD
1187 medium containing 3 μ M CHIR99021, 10 ng/ml human FGF10, 10 ng/mL human
1188 FGF7, 10 ng/ml human BMP4, and 50 nM ATRA for 8 days. At day 20 of
1189 differentiation, the lung organoids were recovered from the Matrigel, and the
1190 resulting suspension of lung organoids (small free-floating clumps) was seeded
1191 onto Matrigel-coated 96-well cell culture plates. The organoids were cultured in
1192 SFD medium containing 50 nM dexamethasone (Selleck, Cat# S1322), 0.1 mM
1193 8-bromo-cAMP (Sigma-Aldrich, Cat# B7880), and 0.1 mM IBMX
1194 (3-isobutyl-1-methylxanthine) (FUJIFILM Wako Pure Chemical, Cat#
1195 099-03411) for an additional 10 days before the antiviral drug experiments.

1196

1197 **Antiviral drug assay using SARS-CoV-2 clinical isolates and iPSC-derived** 1198 **lung organoids**

1199 Antiviral drug assay (**Figure 3**) was performed as previously described²⁹. The
1200 human iPSC-derived lung organoids were infected with either Delta, XBB.1.5,
1201 EG.5.1, or EG.5.1.1 isolate (100 TCID₅₀) at 37°C for 2 h. The cells were
1202 washed with DMEM and cultured in DMEM supplemented with 10% FCS, 1%
1203 PS and the serially diluted Remdesivir (Clinisciences, Cat# A17170), EIDD-1931
1204 (an active metabolite of Molnupiravir; Cell Signalling Technology, Cat# 81178S),
1205 Ensitrelvir (MedChemExpress, Cat# HY-143216), or Nirmatrelvir (PF-07321332;
1206 MedChemExpress, Cat# HY-138687). At 72 h after infection, the culture
1207 supernatants were collected, and viral RNA was quantified using RT-qPCR (see
1208 “RT-qPCR” section below). The assay of each compound was performed in
1209 quadruplicate, and the 50% effective concentration (EC₅₀) was calculated using
1210 Prism 9 software v9.1.1 (GraphPad Software).

1211

1212 **Airway-on-a-chip**

1213 Airway-on-a-chip (**Figures 4D and 4E**) was prepared as previously
1214 described^{19,23,64}. Human lung microvascular endothelial cells (HMVEC-L) were
1215 obtained from Lonza (Cat# CC-2527) and cultured with EGM-2-MV medium
1216 (Lonza, Cat# CC-3202). For preparation of the airway-on-a-chip, first, the bottom
1217 channel of a polydimethylsiloxane (PDMS) device was precoated with
1218 fibronectin (3 μ g/ml, Sigma-Aldrich, Cat# F1141). The microfluidic device was
1219 generated according to our previous report⁶⁵. HMVEC-L cells were suspended
1220 at 5,000,000 cells/ml in EGM2-MV medium. Then, 10 μ l of suspension medium
1221 was injected into the fibronectin-coated bottom channel of the PDMS device.
1222 Then, the PDMS device was turned upside down and incubated. After 1 h, the
1223 device was turned over, and the EGM2-MV medium was added into the bottom
1224 channel. After 4 d, AOs were dissociated and seeded into the top channel. AOs

1225 were generated according to our previous report⁶⁰. AOs were dissociated into
1226 single cells and then suspended at 5,000,000 cells/ml in the AO differentiation
1227 medium. Ten microliter suspension medium was injected into the top channel.
1228 After 1 h, the AO differentiation medium was added to the top channel. In the
1229 infection experiments (**Figure 4D**), the AO differentiation medium containing
1230 either Delta, XBB.1.5, EG.5.1, or EG.5.1.1 isolate (500 TCID₅₀) was inoculated
1231 into the top channel. At 2 h.p.i., the top and bottom channels were washed and
1232 cultured with AO differentiation and EGM2-MV medium, respectively. The
1233 culture supernatants were collected, and viral RNA was quantified using
1234 RT-qPCR (see “RT-qPCR” section above).

1235

1236 **Microfluidic device**

1237 A microfluidic device was generated according to our previous reports^{23,65}.
1238 Briefly, the microfluidic device consisted of two layers of microchannels
1239 separated by a semipermeable membrane. The microchannel layers were
1240 fabricated from PDMS using a soft lithographic method. PDMS prepolymer (Dow
1241 Corning, Cat# SYLGARD 184) at a base to curing agent ratio of 10:1 was cast
1242 against a mold composed of SU-8 2150 (MicroChem, Cat# SU-8 2150) patterns
1243 formed on a silicon wafer. The cross-sectional size of the microchannels was 1
1244 mm in width and 330 μm in height. Access holes were punched through the
1245 PDMS using a 6-mm biopsy punch (Kai Corporation, Cat# BP-L60K) to
1246 introduce solutions into the microchannels. Two PDMS layers were bonded to a
1247 PET membrane containing 3.0-μm pores (Falcon, Cat# 353091) using a thin
1248 layer of liquid PDMS prepolymer as the mortar. PDMS prepolymer was
1249 spin-coated (4,000 rpm for 60 s) onto a glass slide. Subsequently, both the top
1250 and bottom channel layers were placed on the glass slide to transfer the thin
1251 layer of PDMS prepolymer onto the embossed PDMS surfaces. The membrane
1252 was then placed onto the bottom layer and sandwiched with the top layer. The
1253 combined layers were left at room temperature for 1 d to remove air bubbles and
1254 then placed in an oven at 60°C overnight to cure the PDMS glue. The PDMS
1255 devices were sterilized by placing them under UV light for 1 h before the cell
1256 culture.

1257

1258 **SARS-CoV-2 infection**

1259 One day before infection, Vero cells (10,000 cells), VeroE6/TMPRSS2 cells
1260 (10,000 cells), 293-ACE2/TMPRSS2 cells (10,000 cells), and Calu-3 cells
1261 (10,000 cells) were seeded into a 96-well plate. SARS-CoV-2 [1,000 TCID₅₀ for
1262 Vero cells (**Figures 2A and 7D**); 100 TCID₅₀ for VeroE6/TMPRSS2 cells
1263 (**Figures 2B and 7E**); 100 TCID₅₀ for 293-ACE2/TMPRSS2 cells (**Figures 2C**
1264 **and 7F**); and 100 TCID₅₀ for Calu-3 cells (**Figures 2D and 7G**)] was inoculated
1265 and incubated at 37°C for 1 h. The infected cells were washed, and 180 μl of

1266 culture medium was added. The culture supernatant (10 μ l) was harvested at the
1267 indicated timepoints and used for RT-qPCR to quantify the viral RNA copy
1268 number (see “RT-qPCR” section below). In the infection experiments using
1269 AO-ALI model (**Figures 2E and 7H**), the diluted viruses (1,000 TCID₅₀ in
1270 100 μ l) were inoculated onto the apical side of the culture and incubated at
1271 37 $^{\circ}$ C for 1 h. The infected cells were washed, and 100 μ l of AO differentiation
1272 medium was added. The culture supernatant (10 μ l) was harvested at the
1273 indicated timepoints and used for RT-qPCR to quantify the viral RNA copy
1274 number (see “RT-qPCR” section below).

1275 In the infection experiments using iPSC-derived alveolar epithelial cells (**Figure**
1276 **2F**), working viruses were diluted with Opti-MEM (Thermo Fisher Scientific, Cat#
1277 11058021). The diluted viruses (1,000 TCID₅₀ in 100 μ l) were inoculated onto
1278 the apical side of the culture and incubated at 37 $^{\circ}$ C for 1 h. The inoculated
1279 viruses were removed and washed twice with Opti-MEM. For collection of the
1280 viruses, 100 μ l Opti-MEM was applied onto the apical side of the culture and
1281 incubated at 37 $^{\circ}$ C for 10 min. The Opti-MEM was collected and used for
1282 RT-qPCR to quantify the viral RNA copy number (see “RT-qPCR” section
1283 below). The infection experiments using an airway-on-a-chip system (**Figures**
1284 **4D and 4E**) were performed as described above (see “Airway-on-a-chip”
1285 section).

1286

1287 **RT-qPCR**

1288 RT-qPCR was performed as previously described^{14-19,29,57,64}. Briefly, 5 μ l culture
1289 supernatant was mixed with 5 μ l of 2 \times RNA lysis buffer [2% Triton X-100
1290 (Nacalai Tesque, Cat# 35501-15), 50 mM KCl, 100 mM Tris-HCl (pH 7.4), 40%
1291 glycerol, 0.8 U/ μ l recombinant RNase inhibitor (Takara, Cat# 2313B)] and
1292 incubated at room temperature for 10 min. RNase-free water (90 μ l) was added,
1293 and the diluted sample (2.5 μ l) was used as the template for real-time RT-PCR
1294 performed according to the manufacturer’s protocol using One Step TB Green
1295 PrimeScript PLUS RT-PCR kit (Takara, Cat# RR096A) and the following
1296 primers: Forward N, 5'-AGC CTC TTC TCG TTC CTC ATC AC-3'; and Reverse
1297 N, 5'-CCG CCA TTG CCA GCC ATT C-3'. The viral RNA copy number was
1298 standardized with a SARS-CoV-2 direct detection RT-qPCR kit (Takara, Cat#
1299 RC300A). Fluorescent signals were acquired using a QuantStudio 1 Real-Time
1300 PCR system (Thermo Fisher Scientific), QuantStudio 3 Real-Time PCR system
1301 (Thermo Fisher Scientific), QuantStudio 5 Real-Time PCR system (Thermo
1302 Fisher Scientific), StepOne Plus Real-Time PCR system (Thermo Fisher
1303 Scientific), CFX Connect Real-Time PCR Detection system (Bio-Rad), Eco
1304 Real-Time PCR System (Illumina), qTOWER3 G Real-Time System (Analytik
1305 Jena) Thermal Cycler Dice Real Time System III (Takara) or 7500 Real-Time
1306 PCR System (Thermo Fisher Scientific).

1307

1308 **Protein expression and purification of EG.5.1 S protein for cryo-EM**

1309 Protein expression and purification of EG.5.1 S protein were performed as
1310 previously described⁶⁶. Briefly, the expression plasmid, pHLsec, encoding the
1311 EG.5.1 S protein ectodomain bearing six proline substitutions (F817P, A892P,
1312 A899P, A942P, K986P and V987P)⁶⁷ and deletion of the furin cleavage site (i.e.,
1313 RRAR to GSAG substitution) with a T4-foldon domain, were transfected into
1314 HEK293S GnTI(-) cells. Expressed proteins in the cell-culture supernatant were
1315 purified using a cOmplete His-Tag Purification Resin (Roche, Cat# 5893682001)
1316 affinity column, followed by Superose 6 Increase 10/300 GL size-exclusion
1317 chromatography (Cytiva, Cat# 29091596) with calcium- and magnesium-free
1318 PBS buffer.

1319

1320 **Cryo-EM sample preparation and data collection**

1321 The solution of EG.5.1 S protein was incubated at 37 °C for 1 h before cryo-EM
1322 grid preparation. The samples were applied to a Quantifoil R2/2 Cu 300 mesh
1323 grid (Quantifoil Micro Tools GmbH), which had been freshly glow-discharged for
1324 60 s at 10 mA using PIB-10 (Vacuum Device). The samples were plunged into
1325 liquid ethane using a Vitrobot mark IV (Thermo Fisher Scientific) with the
1326 following settings: temperature 18°C, humidity 100%, blotting time 5 s, and
1327 blotting force 5.

1328 Movies were collected on a Krios G4 (Thermo Fisher Scientific) operated
1329 at 300 kV with a K3 direct electron detector (Gatan) at a nominal magnification of
1330 130,000 (0.67 Å per physical pixel), using a GIF-Biocontinuum energy filter
1331 (Gatan) with a 20 eV slit width. Each micrograph was collected with a total
1332 exposure of 1.5 s and a total dose of 50.1 e/Å² over 50 frames. A total of 3,285
1333 movies were collected at a nominal defocus range of 0.8 – 1.8 µm using EPU
1334 software (Thermo Fisher Scientific).

1335

1336 **Cryo-EM data processing**

1337 All datasets were processed in cryoSPARC v4.3.1⁶⁸. Movie frames were aligned,
1338 dose-weighted, and CTF-estimated using Patch Motion correction and Patch
1339 CTF. 899,573 particles were blob-picked and reference-free 2D classification (K
1340 = 150, batch = 200, Iteration = 30) was performed to remove junk particles.
1341 348,621 particles were used for initial model reconstruction and heterogeneous
1342 refinement. Two classes of closed states (closed-1 and closed-2) with different
1343 RBD orientations and one class of 1-up state were separated in heterogeneous
1344 refinement. The closed-1 state was processed by non-uniform refinement with
1345 C3 symmetry and CTF refinement to generate the final maps. Since the density
1346 of the RBD was unclear for the closed-2 and the 1-up states, additional
1347 processing steps were performed for these states. For the closed-2 state, once

1348 the particles were aligned with non-uniform refinement followed by aligned
1349 particles were symmetry-expanded under C3 symmetry operation. 3D
1350 classification (K = 4, force hard classification, input mode = simple) focused on
1351 the RBD without alignment was performed, and selected classes that the density
1352 of RBD was clearly resolved. A final map of closed-2 state was reconstructed
1353 with non-uniform refinement with C3 symmetry. For 1-up state, 3D classification
1354 (K = 4, force hard classification, input mode = simple) focused on the down RBD
1355 and up RBD without alignment was performed, and selected classes that the
1356 density of up RBD was clearly resolved. A final map of 1-up state was
1357 reconstructed with non-uniform refinement with C1 symmetry. C1 for 1-up state
1358 after removing duplicate particles. To support model building, a local refinement
1359 focusing on down RBD in closed-2 and down and up RBD in 1-up states was
1360 carried out.

1361 The reported global resolutions are based on the gold-standard Fourier
1362 shell correlation curves (FSC = 0.143) criteria. Local resolutions were calculated
1363 with cryoSPARC⁶⁹. Workflows of data processing were shown in
1364 **Supplementary Figure 1A**. Figures related to data processing and
1365 reconstructed maps were prepared with UCSF Chimera v1.17.1⁷⁰ and UCSF
1366 Chimera X v1.6.1⁷¹.

1367

1368 **Cryo-EM model building and analysis**

1369 Structures of SARS-CoV-2 XBB.1 S protein closed-1 state (PDB: 8IOS¹) or
1370 closed-2 state (PDB: 8IOT) were fitted to the corresponding maps using UCSF
1371 Chimera. Iterative rounds of manual fitting in Coot v0.9.6⁷² and real-space
1372 refinement in Phenix v1.20⁷³ were carried out to improve non-ideal rotamers,
1373 bond angles, and Ramachandran outliers. The final model was validated with
1374 MolProbity⁷⁴. The structure models shown in surface, ribbon and stick
1375 presentation in figures were prepared with PyMOL v2.5.0
1376 (<http://pymol.sourceforge.net>).

1377

1378 **Animal experiments**

1379 Animal experiments (**Figure 6** and **Supplementary Figure 2**) were performed
1380 as previously described^{1,5,15-19,22}. Syrian hamsters (male, 4 weeks old) were
1381 purchased from Japan SLC Inc. (Shizuoka, Japan). For the virus infection
1382 experiments, hamsters were anesthetized by intramuscular injection of a mixture
1383 of 0.15 mg/kg medetomidine hydrochloride (Domitor[®], Nippon Zenyaku Kogyo),
1384 2.0 mg/kg midazolam (Dormicum[®], FUJIFILM WAKO, Cat# 135-13791) and 2.5
1385 mg/kg butorphanol (Vetorphale[®], Meiji Seika Pharma) or 0.15 mg/kg
1386 medetomidine hydrochloride, 4.0 mg/kg alphaxalone (Alfaxan[®], Jurox) and 2.5
1387 mg/kg butorphanol. EG.5.1, EG.5.1.1, XBB1.5, Delta (10,000 TCID₅₀ in 100 µl),
1388 or saline (100 µl) were intranasally inoculated under anesthesia. Oral swabs

1389 were collected at the indicated timepoints. Body weight was recorded daily by 7
1390 d.p.i. Enhanced pause (Penh), the ratio of time to peak expiratory flow relative
1391 to the total expiratory time (Rpef) were measured every day until 7 d.p.i. of the
1392 EG.5.1-, EG.5.1.1-, XBB.1.5-, and Delta-infected hamsters (see below). Lung
1393 tissues were anatomically collected at 2 and 5 d.p.i. The viral RNA load in the
1394 oral swabs and respiratory tissues was determined by RT-qPCR. These tissues
1395 were also used for IHC and histopathological analyses (see below).

1396

1397 **Lung function test**

1398 Lung function tests (**Figure 6A**) were routinely performed as previously
1399 described^{1,5,15,17-19,22}. The two respiratory parameters (Penh and Rpef) were
1400 measured by using a Buxco Small Animal Whole Body Plethysmography system
1401 (DSI) according to the manufacturer's instructions. In brief, a hamster was
1402 placed in an unrestrained plethysmography chamber and allowed to acclimatize
1403 for 30 s. Then, data were acquired over a 2.5-minute period by using FinePointe
1404 Station and Review software v2.9.2.12849 (DSI).

1405

1406 **Immunohistochemistry**

1407 Immunohistochemistry (IHC) (**Figure 6C** and **Supplementary Figure 2**) was
1408 performed as previously described^{1,5,15-19,22} using an Autostainer Link 48 (Dako).
1409 The deparaffinized sections were exposed to EnVision FLEX target retrieval
1410 solution high pH (Agilent, Cat# K8004) for 20 m at 97°C for activation, and a
1411 mouse anti-SARS-CoV-2 N monoclonal antibody (clone 1035111, R&D Systems,
1412 Cat# MAB10474-SP, 1:400) was used as a primary antibody. The sections were
1413 sensitized using EnVision FLEX for 15 m and visualized by peroxidase-based
1414 enzymatic reaction with 3,3'-diaminobenzidine tetrahydrochloride (Dako, Cat#
1415 DM827) as substrate for 5 m. The N protein positivity was evaluated by
1416 certificated pathologists as previously described. Images were incorporated as
1417 virtual slides by NDP.scan software v3.2.4 (Hamamatsu Photonics). The
1418 N-protein positivity was measured as the area using Fiji software v2.2.0
1419 (ImageJ).

1420

1421 **H&E staining**

1422 H&E staining (**Figure 6D** and **Supplementary Figure 3**) was performed as
1423 previously described^{1,5,15-19,22}. Briefly, excised animal tissues were fixed with
1424 10% formalin neutral buffer solution and processed for paraffin embedding. The
1425 paraffin blocks were sectioned at a thickness of 3 µm and then mounted on
1426 MAS-GP-coated glass slides (Matsunami Glass, Cat# S9901). H&E staining was
1427 performed according to a standard protocol.

1428

1429 **Histopathological scoring**

1430 Histopathological scoring (**Figure 6E**) was performed as previously
1431 described^{1,5,15-19,22}. Pathological features, including (i) bronchitis or bronchiolitis,
1432 (ii) hemorrhage with congestive edema, (iii) alveolar damage with epithelial
1433 apoptosis and macrophage infiltration, (iv) hyperplasia of type II pneumocytes,
1434 and (v) the area of hyperplasia of large type II pneumocytes, were evaluated in
1435 each hamsters by certified pathologists, and the degree of these pathological
1436 findings was arbitrarily scored using a four-tiered system as 0 (negative), 1
1437 (weak), 2 (moderate), and 3 (severe). The “large type II pneumocytes” are type II
1438 pneumocytes with hyperplasia exhibiting more than 10- μ m-diameter nuclei. We
1439 described “large type II pneumocytes” as one of the notable histopathological
1440 features of SARS-CoV-2 infection in our previous studies. The total histological
1441 score is the sum of these five indices.

1442

1443 **Transfection, western blotting, SeV Infection and reporter assay**

1444 HEK293 cells were transfected using PEI Max (Polysciences) according to the
1445 manufacturer’s protocol. For Western blotting, cells (in 12 well) were
1446 cotransfected with the pLVX-EF1alpha-IRES-Puro-based 2 \times Strep-tagged
1447 expression plasmids (12.5, 50, 200 or 800 ng for **Figure 7B**; 300, 600 or 900 ng
1448 for **Figure 7D**) together with an empty vector (normalized to 1 μ g per well). For
1449 luciferase reporter assay, cells (in 96 well) were cotransfected with 10 ng of
1450 either p125Luc (expressing firefly luciferase driven by human IFNB1 promoter;
1451 kindly provided by Dr. Takashi Fujita)⁷⁵ and the
1452 pLVX-EF1alpha-IRES-Puro-based 2 \times Strep-tagged expression plasmids (1.25, 5,
1453 20 or 80 ng for Figures 7B; 30, 60 or 90 ng for **Figure 7D**). The amounts of
1454 transfected plasmids were normalized to 100 ng per well. At 24 h post
1455 transfection, SeV (strain Cantell, clone cCdi; GenBank accession no.
1456 AB855654)⁷⁶ was inoculated into the transfected cells at multiplicity of infection
1457 (MOI) 100.

1458 The luciferase reporter assay was performed 24 h.p.i. as previously
1459 described^{28,77}. Briefly, 50 μ l cell lysate was applied to a 96-well plate (Nunc), and
1460 the firefly luciferase activity was measured using a PicaGene BrilliantStar-LT
1461 luciferase assay system (Toyo-b-net), and the input for the luciferase assay was
1462 normalized by using a CellTiter-Glo 2.0 assay kit (Promega) following the
1463 manufacturers’ instructions. For this assay, a GloMax Explorer Multimode
1464 Microplate Reader 3500 (Promega) was used.

1465 Western Blotting was performed as previously described^{28,77}. Briefly,
1466 transfected cells were lysed with RIPA buffer (25 mM HEPES [pH 7.4], 50 mM
1467 NaCl, 1 mM MgCl₂, 50 mM ZnCl₂, 10% glycerol, 1% Triton X-100) containing a
1468 protease inhibitor cocktail (Roche). For blotting, anti-Strep-tag II antibody
1469 (Abcam, Cat# ab76949) and anti- α -Tubulin antibody (Sigma, Cat# T9026) were
1470 used as primary antibody. Horseradish peroxidase-conjugated anti-mouse IgG

1471 antibody (Cell Signaling, Cat# 7076) and Horseradish peroxidase-conjugated
1472 anti-rabbit IgG antibody (Cell Signaling, Cat# 7074) were used as secondary
1473 antibody.

1474

1475 **Statistics and reproducibility**

1476 Statistical significance was tested using a two-sided Mann–Whitney *U* test, a
1477 two-sided Student's *t* test, a two-sided Welch's *t* test, or a two-sided paired *t*-test
1478 unless otherwise noted. The tests above were performed using Prism 9 software
1479 v9.1.1 (GraphPad Software).

1480 In the time-course experiments (**Figure 2A–F, 4C–D, 6A–B, E, 6D–H,**
1481 **7D–H**), a multiple regression analysis including experimental conditions (i.e., the
1482 types of infected viruses) as explanatory variables and timepoints as qualitative
1483 control variables was performed to evaluate the difference between
1484 experimental conditions thorough all timepoints. The initial time point was
1485 removed from the analysis. The *P* value was calculated by a two-sided Wald test.
1486 Subsequently, familywise error rates (FWERs) were calculated by the Holm
1487 method. These analyses were performed on R v4.2.1
1488 (<https://www.r-project.org/>).

1489 In **Figure 4C–D, and Supplementary Figure 1**, photographs shown
1490 are the representative areas of at least two independent experiments by using
1491 four hamsters at each timepoint.

1492

1493 **Data availability**

1494 Surveillance datasets of SARS-CoV-2 isolates are available from the GISAID
1495 database (<https://www.gisaid.org>; EPI_SET_231018pe, EPI_SET_231003ue,
1496 and EPI_SET_231003vx). The supplemental table for each GISAID dataset is
1497 available in the GitHub repository (<https://github.com/TheSatoLab/EG.5.1>). The
1498 atomic coordinates and cryo-EM maps for the structures of the EG.5.1 S
1499 protein alone closed state 1 (8WMF, EMD-37651), closed state 2 (8WMD,
1500 EMD-37650), 1-up (EMD-37648) are available in the Protein Data Bank
1501 (www.rcsb.org) and Electron Microscopy Data Bank (www.ebi.ac.uk/emdb/).

1502

1503 **Code availability**

1504 The computational codes used in the present study are available in the GitHub
1505 repository (<https://github.com/TheSatoLab/EG.5.1>).

1506 **References**

- 1507 1. Tamura, T., Ito, J., Uriu, K., et al. (2023). Virological characteristics of the
1508 SARS-CoV-2 XBB variant derived from recombination of two Omicron
1509 subvariants. *Nat Commun* **14**, 2800.
- 1510 2. Uriu, K., Ito, J., Zahradnik, J., et al. (2023). Enhanced transmissibility,
1511 infectivity, and immune resistance of the SARS-CoV-2 omicron XBB.1.5
1512 variant. *Lancet Infect Dis* **23**, 280-281, [10.1016/S1473-3099\(23\)00051-8](https://doi.org/10.1016/S1473-3099(23)00051-8).
- 1513 3. WHO (2023). "Tracking SARS-CoV-2 variants (August 17, 2023)"
1514 <https://www.who.int/en/activities/tracking-SARS-CoV-2-variants>.
- 1515 4. Kaku, Y., Kosugi, Y., Uriu, K., et al. (2023). Antiviral efficacy of the
1516 SARS-CoV-2 XBB breakthrough infection sera against omicron
1517 subvariants including EG.5. *Lancet Infect Dis*
1518 [10.1016/S1473-3099\(23\)00553-4](https://doi.org/10.1016/S1473-3099(23)00553-4).
- 1519 5. Ito, J., Suzuki, R., Uriu, K., et al. (2023). Convergent evolution of the
1520 SARS-CoV-2 Omicron subvariants leading to the emergence of BQ.1.1
1521 variant. *Nat Commun* **14**, 2671.
- 1522 6. Bloom, J.D., and Neher, R.A. (2023). Fitness effects of mutations to
1523 SARS-CoV-2 proteins. *Virus Evol* **9**, vead055, [10.1093/ve/vead055](https://doi.org/10.1093/ve/vead055).
- 1524 7. Thorne, L.G., Bouhaddou, M., Reuschl, A.K., et al. (2022). Evolution of
1525 enhanced innate immune evasion by SARS-CoV-2. *Nature* **602**, 487-495,
1526 [10.1038/s41586-021-04352-y](https://doi.org/10.1038/s41586-021-04352-y).
- 1527 8. Han, L., Zhuang, M.W., Deng, J., et al. (2021). SARS-CoV-2 ORF9b
1528 antagonizes type I and III interferons by targeting multiple components of
1529 the RIG-I/MDA-5-MAVS, TLR3-TRIF, and cGAS-STING signaling
1530 pathways. *J Med Virol* **93**, 5376-5389, [10.1002/jmv.27050](https://doi.org/10.1002/jmv.27050).
- 1531 9. Wu, J., Shi, Y., Pan, X., et al. (2021). SARS-CoV-2 ORF9b inhibits
1532 RIG-I-MAVS antiviral signaling by interrupting K63-linked ubiquitination of
1533 NEMO. *Cell Rep* **34**, 108761, [10.1016/j.celrep.2021.108761](https://doi.org/10.1016/j.celrep.2021.108761).
- 1534 10. Jiang, H.W., Zhang, H.N., Meng, Q.F., et al. (2020). SARS-CoV-2 Orf9b
1535 suppresses type I interferon responses by targeting TOM70. *Cell Mol
1536 Immunol* **17**, 998-1000, [10.1038/s41423-020-0514-8](https://doi.org/10.1038/s41423-020-0514-8).
- 1537 11. Wang, Q., Guo, Y., Zhang, R.M., et al. (2023). Antibody neutralisation of
1538 emerging SARS-CoV-2 subvariants: EG.5.1 and XBC.1.6. *Lancet Infect
1539 Dis* **23**, e397-e398, [10.1016/S1473-3099\(23\)00555-8](https://doi.org/10.1016/S1473-3099(23)00555-8).
- 1540 12. Zhang, L., Kempf, A., Nehlmeier, I., et al. (2023). Neutralisation sensitivity
1541 of SARS-CoV-2 lineages EG.5.1 and XBB.2.3. *Lancet Infect Dis* **23**,
1542 e391-e392, [10.1016/S1473-3099\(23\)00547-9](https://doi.org/10.1016/S1473-3099(23)00547-9).
- 1543 13. Yamasoba, D., Uriu, K., Plianpaisuk, A., et al. (2023). Virological
1544 characteristics of the SARS-CoV-2 omicron XBB.1.16 variant. *Lancet
1545 Infect Dis* **23**, 655-656, [10.1016/S1473-3099\(23\)00278-5](https://doi.org/10.1016/S1473-3099(23)00278-5).
- 1546 14. Motozono, C., Toyoda, M., Zahradnik, J., et al. (2021). SARS-CoV-2

- 1547 spike L452R variant evades cellular immunity and increases infectivity.
1548 Cell Host Microbe **29**, 1124-1136, 10.1016/j.chom.2021.06.006.
- 1549 15. Suzuki, R., Yamasoba, D., Kimura, I., et al. (2022). Attenuated
1550 fusogenicity and pathogenicity of SARS-CoV-2 Omicron variant. Nature
1551 **603**, 700-705, 10.1038/s41586-022-04462-1.
- 1552 16. Saito, A., Irie, T., Suzuki, R., et al. (2022). Enhanced fusogenicity and
1553 pathogenicity of SARS-CoV-2 Delta P681R mutation. Nature **602**,
1554 300-306, 10.1038/s41586-021-04266-9.
- 1555 17. Yamasoba, D., Kimura, I., Nasser, H., et al. (2022). Virological
1556 characteristics of the SARS-CoV-2 Omicron BA.2 spike. Cell **185**,
1557 2103-2115.e2119, 10.1016/j.cell.2022.04.035.
- 1558 18. Kimura, I., Yamasoba, D., Tamura, T., et al. (2022). Virological
1559 characteristics of the novel SARS-CoV-2 Omicron variants including BA.4
1560 and BA.5. Cell **185**, 3992-4007.e3916.
- 1561 19. Saito, A., Tamura, T., Zahradnik, J., et al. (2022). Virological
1562 characteristics of the SARS-CoV-2 Omicron BA.2.75 variant. Cell Host
1563 Microbe **30**, 1540–1555.e1515, 10.1016/j.chom.2022.10.003.
- 1564 20. Nasser, H., Shimizu, R., Ito, J., et al. (2022). Monitoring fusion kinetics of
1565 viral and target cell membranes in living cells using a SARS-CoV-2
1566 spike-protein-mediated membrane fusion assay. STAR Protoc **3**, 101773,
1567 10.1016/j.xpro.2022.101773.
- 1568 21. Begum, M.M., Ichihara, K., Takahashi, O., et al. (2023). Virological
1569 characteristics correlating with SARS-CoV-2 spike protein fusogenicity.
1570 BioRxiv doi: <https://doi.org/10.1101/2023.1110.1103.560628>.
- 1571 22. Tamura, T., Irie, T., Deguchi, S., et al. (2023). Virological characteristics
1572 of the SARS-CoV-2 XBB.1.5 variant. BioRxiv doi:
1573 <https://doi.org/10.1101/2023.1108.1116.553332>.
- 1574 23. Hashimoto, R., Takahashi, J., Shirakura, K., et al. (2022). SARS-CoV-2
1575 disrupts the respiratory vascular barrier by suppressing Claudin-5
1576 expression. Sci Adv **8**, eabo6783, doi: 10.1126/sciadv.abo6783.
- 1577 24. Cao, Y., Song, W., Wang, L., et al. (2022). Characterization of the
1578 enhanced infectivity and antibody evasion of Omicron BA.2.75. Cell Host
1579 Microbe **30**, 1527-1539 e1525, 10.1016/j.chom.2022.09.018.
- 1580 25. Zhao, Z., Zhou, J., Tian, M., et al. (2022). Omicron SARS-CoV-2
1581 mutations stabilize spike up-RBD conformation and lead to a
1582 non-RBM-binding monoclonal antibody escape. Nat Commun **13**, 4958,
1583 10.1038/s41467-022-32665-7.
- 1584 26. Xu, C., Wang, Y., Liu, C., et al. (2021). Conformational dynamics of
1585 SARS-CoV-2 trimeric spike glycoprotein in complex with receptor ACE2
1586 revealed by cryo-EM. Sci Adv **7**, 10.1126/sciadv.abe5575.
- 1587 27. Gordon, D.E., Jang, G.M., Bouhaddou, M., et al. (2020). A SARS-CoV-2

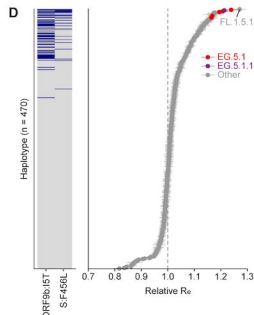
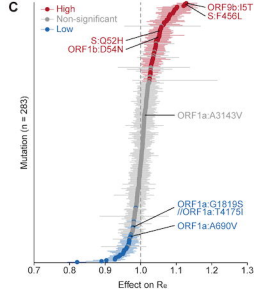
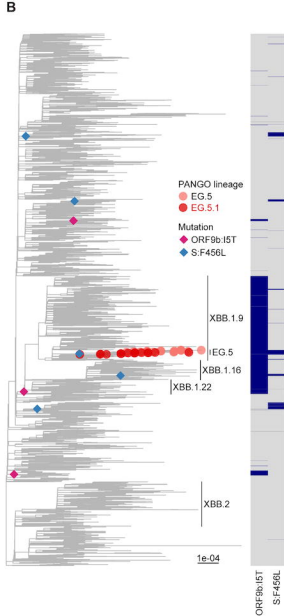
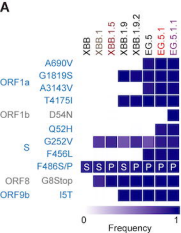
- 1588 protein interaction map reveals targets for drug repurposing. *Nature* **583**,
1589 459-468, 10.1038/s41586-020-2286-9.
- 1590 28. Kimura, I., Konno, Y., Uriu, K., et al. (2021). Sarbecovirus ORF6 proteins
1591 hamper induction of interferon signaling. *Cell Rep* **34**, 108916,
1592 10.1016/j.celrep.2021.108916.
- 1593 29. Meng, B., Abdullahi, A., Ferreira, I.A.T.M., et al. (2022). Altered
1594 TMPRSS2 usage by SARS-CoV-2 Omicron impacts tropism and
1595 fusogenicity. *Nature* **603**, 706-714, 10.1038/s41586-022-04474-x.
- 1596 30. Yamasoba, D., Kosugi, Y., Kimura, I., et al. (2022). Neutralisation
1597 sensitivity of SARS-CoV-2 omicron subvariants to therapeutic monoclonal
1598 antibodies. *Lancet Infect Dis* **22**, 942-943,
1599 10.1016/S1473-3099(22)00365-6.
- 1600 31. Kimura, I., Yamasoba, D., Nasser, H., et al. (2022). The SARS-CoV-2
1601 spike S375F mutation characterizes the Omicron BA.1 variant. *iScience*
1602 **25**, 105720, 10.1016/j.isci.2022.105720.
- 1603 32. Kimura, I.Y., Daichi Tamura, Tomokazu Nao, Naganori Oda,
1604 Yoshitaka Mitoma Shuya Ito, Jumpei Nasser, Hesham Zahradnik,
1605 Jiri Uriu, Keiya Fujita, Shigeru Kosugi, Yusuke Wang, Lei Tsuda,
1606 Masumi Kishimoto, Mai Ito, Hayato Suzuki, Rigel Shimizu, Ryo
1607 Begum, MST Monira Yoshimatsu, Kumiko Sasaki, Jiei
1608 Sasaki-Tabata, Kaori Yamamoto, Yuki Nagamoto, Tetsuharu
1609 Kanamune, Jun Kobiyama, Kouji Asakura, Hiroyuki Nagashima,
1610 Mami Sadamasu, Kenji Yoshimura, Kazuhisa Kuramochi, Jin
1611 Schreiber, Gideon Ishii, Ken J Hashiguchi, Takao The Genotype to
1612 Phenotype Japan (G2P-Japan) Consortium, Ikeda, Terumasa Saito,
1613 Akatsuki Fukuhara, Takasuke Tanaka, Shinya Matsuno, Keita
1614 Sato, Kei (2022). Virological characteristics of the novel SARS-CoV-2
1615 Omicron variants including BA.2.12.1, BA.4 and BA.5.
1616 doi.org/10.1101/2022.05.26.493539.
- 1617 33. Ito, J., Suzuki, R., Uriu, K., et al. (2023). Convergent evolution of
1618 SARS-CoV-2 Omicron subvariants leading to the emergence of BQ.1.1
1619 variant. *Nat Commun* **14**, 2671, 10.1038/s41467-023-38188-z.
- 1620 34. Tamura, T., Ito, J., Uriu, K., et al. (2023). Virological characteristics of the
1621 SARS-CoV-2 XBB variant derived from recombination of two Omicron
1622 subvariants. *Nat Commun* **14**, 2800, 10.1038/s41467-023-38435-3.
- 1623 35. Tamura, T., Yamasoba, D., Oda, Y., et al. (2023). Comparative
1624 pathogenicity of SARS-CoV-2 Omicron subvariants including BA.1, BA.2,
1625 and BA.5. *Commun Biol* **6**, 772, 10.1038/s42003-023-05081-w.
- 1626 36. Ozono, S., Zhang, Y., Ode, H., et al. (2021). SARS-CoV-2 D614G spike
1627 mutation increases entry efficiency with enhanced ACE2-binding affinity.
1628 *Nat Commun* **12**, 848, 10.1038/s41467-021-21118-2.

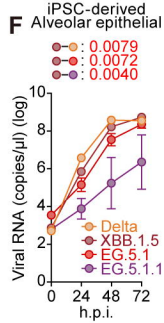
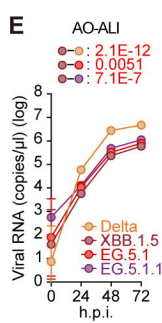
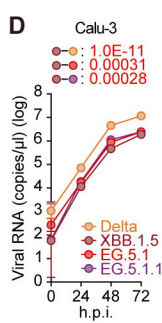
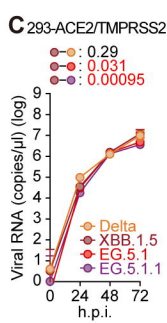
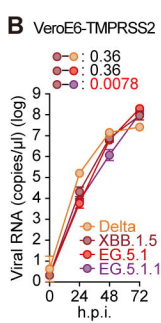
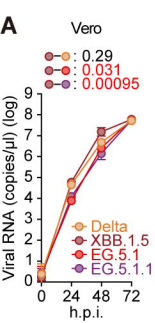
- 1629 37. Ferreira, I., Kemp, S.A., Datir, R., et al. (2021). SARS-CoV-2 B.1.617
1630 mutations L452R and E484Q are not synergistic for antibody evasion. *J.*
1631 *Infect. Dis.* **224**, 989-994, 10.1093/infdis/jiab368.
- 1632 38. Matsuyama, S., Nao, N., Shirato, K., et al. (2020). Enhanced isolation of
1633 SARS-CoV-2 by TMPRSS2-expressing cells. *Proc Natl Acad Sci U S A*
1634 **117**, 7001-7003, 10.1073/pnas.2002589117.
- 1635 39. Fujita, S., Kosugi, Y., Kimura, I., et al. (2022). Structural Insight into the
1636 Resistance of the SARS-CoV-2 Omicron BA.4 and BA.5 Variants to
1637 Cilgavimab. *Viruses* **14**, 2677.
- 1638 40. Chen, S., Zhou, Y., Chen, Y., and Gu, J. (2018). fastp: an ultra-fast
1639 all-in-one FASTQ preprocessor. *Bioinformatics* **34**, i884-i890,
1640 10.1093/bioinformatics/bty560.
- 1641 41. Li, H., and Durbin, R. (2009). Fast and accurate short read alignment with
1642 Burrows-Wheeler transform. *Bioinformatics* **25**, 1754-1760,
1643 10.1093/bioinformatics/btp324.
- 1644 42. Li, H., Handsaker, B., Wysoker, A., et al. (2009). The sequence
1645 alignment/map format and SAMtools. *Bioinformatics* **25**, 2078-2079,
1646 10.1093/bioinformatics/btp352.
- 1647 43. Cingolani, P., Platts, A., Wang le, L., et al. (2012). A program for
1648 annotating and predicting the effects of single nucleotide polymorphisms,
1649 SnpEff: SNPs in the genome of *Drosophila melanogaster* strain w1118;
1650 iso-2; iso-3. *Fly (Austin)* **6**, 80-92, 10.4161/fly.19695.
- 1651 44. Khare, S., Gurry, C., Freitas, L., et al. (2021). GISAID's role in pandemic
1652 response. *China CDC Wkly* **3**, 1049-1051, 10.46234/ccdcw2021.255.
- 1653 45. Aksamentov, I., Roemer, C., Hodcroft, E., and Neher, R. (2021).
1654 Nextclade: clade assignment, mutation calling and quality control for viral
1655 genomes. *The Journal of Open Source Software* **6**, 3773,
1656 <https://doi.org/10.21105/joss.03773>.
- 1657 46. Moshiri, N. (2021). ViralMSA: massively scalable reference-guided
1658 multiple sequence alignment of viral genomes. *Bioinformatics* **37**,
1659 714-716, 10.1093/bioinformatics/btaa743.
- 1660 47. Capella-Gutierrez, S., Silla-Martinez, J.M., and Gabaldon, T. (2009).
1661 trimAl: a tool for automated alignment trimming in large-scale
1662 phylogenetic analyses. *Bioinformatics* **25**, 1972-1973,
1663 10.1093/bioinformatics/btp348.
- 1664 48. Minh, B.Q., Schmidt, H.A., Chernomor, O., et al. (2020). IQ-TREE 2: New
1665 Models and Efficient Methods for Phylogenetic Inference in the Genomic
1666 Era. *Mol Biol Evol* **37**, 1530-1534, 10.1093/molbev/msaa015.
- 1667 49. Kalyaanamoorthy, S., Minh, B.Q., Wong, T.K.F., et al. (2017).
1668 ModelFinder: fast model selection for accurate phylogenetic estimates.
1669 *Nat Methods* **14**, 587-589, 10.1038/nmeth.4285.

- 1670 50. Hoang, D.T., Chernomor, O., von Haeseler, A., et al. (2018). UFBoot2:
1671 Improving the Ultrafast Bootstrap Approximation. *Mol Biol Evol* **35**,
1672 518-522, 10.1093/molbev/msx281.
- 1673 51. Paradis, E., and Schliep, K. (2019). ape 5.0: an environment for modern
1674 phylogenetics and evolutionary analyses in R. *Bioinformatics* **35**, 526-528,
1675 10.1093/bioinformatics/bty633.
- 1676 52. Yu, G. (2020). Using ggtree to visualize data on tree-like structures. *Curr*
1677 *Protoc Bioinformatics* **69**, e96, 10.1002/cpbi.96.
- 1678 53. R Core Team (2023). "R: A language and environment for statistical
1679 computing. R Foundation for Statistical Computing, Vienna, Austria."
1680 <https://www.R-project.org/>.
- 1681 54. Zahradnik, J., Kolarova, L., Peleg, Y., et al. (2019). Flexible regions
1682 govern promiscuous binding of IL-24 to receptors IL-20R1 and IL-22R1.
1683 *FEBS J.* **286**, 3858-3873, 10.1111/febs.14945.
- 1684 55. Dejnirattisai, W., Huo, J., Zhou, D., et al. (2022). SARS-CoV-2
1685 Omicron-B.1.1.529 leads to widespread escape from neutralizing
1686 antibody responses. *Cell* **185**, 467-484 e415, 10.1016/j.cell.2021.12.046.
- 1687 56. Torii, S., Ono, C., Suzuki, R., et al. (2021). Establishment of a reverse
1688 genetics system for SARS-CoV-2 using circular polymerase extension
1689 reaction. *Cell Rep* **35**, 109014.
- 1690 57. Kimura, I., Yamasoba, D., Nasser, H., et al. (2022). SARS-CoV-2 spike
1691 S375F mutation characterizes the Omicron BA.1 variant. *BioRxiv* doi:
1692 <https://doi.org/10.1101/2022.1104.1103.486864>.
- 1693 58. Reed, L.J., and Muench, H. (1938). A simple method of estimating fifty
1694 percent endpoints. *Am J Hygiene* **27**, 493-497.
- 1695 59. Kondo, N., Miyauchi, K., and Matsuda, Z. (2011). Monitoring
1696 viral-mediated membrane fusion using fluorescent reporter methods. *Curr*
1697 *Protoc Cell Biol* **Chapter 26**, Unit 26 29,
1698 10.1002/0471143030.cb2609s50.
- 1699 60. Sano, E., Suzuki, T., Hashimoto, R., et al. (2022). Cell response analysis
1700 in SARS-CoV-2 infected bronchial organoids. *Commun Biol* **5**, 516,
1701 10.1038/s42003-022-03499-2.
- 1702 61. Yamamoto, Y., Gotoh, S., Korogi, Y., et al. (2017). Long-term expansion
1703 of alveolar stem cells derived from human iPS cells in organoids. *Nat*
1704 *Methods* **14**, 1097-1106, 10.1038/nmeth.4448.
- 1705 62. Konishi, S., Gotoh, S., Tateishi, K., et al. (2016). Directed induction of
1706 functional multi-ciliated cells in proximal airway epithelial spheroids from
1707 human pluripotent stem cells. *Stem Cell Reports* **6**, 18-25,
1708 10.1016/j.stemcr.2015.11.010.
- 1709 63. Gotoh, S., Ito, I., Nagasaki, T., et al. (2014). Generation of alveolar
1710 epithelial spheroids via isolated progenitor cells from human pluripotent

- 1711 stem cells. *Stem Cell Reports* **3**, 394-403, 10.1016/j.stemcr.2014.07.005.
- 1712 64. Tamura, T., Yamasoba, D., Oda, Y., et al. (2022). Comparative
1713 pathogenicity of SARS-CoV-2 Omicron subvariants including BA.1, BA.2,
1714 and BA.5. *BioRxiv* doi: <https://doi.org/10.1101/2022.1108.1105.502758>.
- 1715 65. Deguchi, S., Tsuda, M., Kosugi, K., et al. (2021). Usability of
1716 polydimethylsiloxane-based microfluidic devices in pharmaceutical
1717 research using human hepatocytes. *ACS Biomater Sci Eng* **7**, 3648-3657,
1718 10.1021/acsbiomaterials.1c00642.
- 1719 66. Hashiguchi, T., Ose, T., Kubota, M., et al. (2011). Structure of the
1720 measles virus hemagglutinin bound to its cellular receptor SLAM. *Nat.*
1721 *Struct. Mol. Biol.* **18**, 135-141, 10.1038/nsmb.1969.
- 1722 67. Hsieh, C.L., Goldsmith, J.A., Schaub, J.M., et al. (2020). Structure-based
1723 design of prefusion-stabilized SARS-CoV-2 spikes. *Science* **369**,
1724 1501-1505, 10.1126/science.abd0826.
- 1725 68. Punjani, A., Rubinstein, J.L., Fleet, D.J., and Brubaker, M.A. (2017).
1726 cryoSPARC: algorithms for rapid unsupervised cryo-EM structure
1727 determination. *Nat Methods* **14**, 290-296, 10.1038/nmeth.4169.
- 1728 69. Cardone, G., Heymann, J.B., and Steven, A.C. (2013). One number does
1729 not fit all: mapping local variations in resolution in cryo-EM
1730 reconstructions. *J Struct Biol* **184**, 226-236, 10.1016/j.jsb.2013.08.002.
- 1731 70. Pettersen, E.F., Goddard, T.D., Huang, C.C., et al. (2004). UCSF
1732 Chimera—a visualization system for exploratory research and analysis. *J*
1733 *Comput Chem* **25**, 1605-1612, 10.1002/jcc.20084.
- 1734 71. Goddard, T.D., Huang, C.C., Meng, E.C., et al. (2018). UCSF ChimeraX:
1735 Meeting modern challenges in visualization and analysis. *Protein Sci* **27**,
1736 14-25, 10.1002/pro.3235.
- 1737 72. Emsley, P., Lohkamp, B., Scott, W.G., and Cowtan, K. (2010). Features
1738 and development of Coot. *Acta Crystallogr D Biol Crystallogr* **66**, 486-501,
1739 10.1107/S0907444910007493.
- 1740 73. Liebschner, D., Afonine, P.V., Baker, M.L., et al. (2019). Macromolecular
1741 structure determination using X-rays, neutrons and electrons: recent
1742 developments in Phenix. *Acta Crystallogr D Struct Biol* **75**, 861-877,
1743 10.1107/S2059798319011471.
- 1744 74. Williams, C.J., Headd, J.J., Moriarty, N.W., et al. (2018). MolProbity: More
1745 and better reference data for improved all-atom structure validation.
1746 *Protein Sci* **27**, 293-315, 10.1002/pro.3330.
- 1747 75. Fujita, T., Nolan, G.P., Liou, H.C., et al. (1993). The candidate
1748 proto-oncogene bcl-3 encodes a transcriptional coactivator that activates
1749 through NF-kappa B p50 homodimers. *Genes Dev.* **7**, 1354-1363,
1750 10.1101/gad.7.7b.1354.
- 1751 76. Yoshida, A., Kawabata, R., Honda, T., et al. (2018). A single amino acid

1752 substitution within the paramyxovirus Sendai virus nucleoprotein is a
1753 critical determinant for production of interferon-beta-inducing
1754 copyback-type defective interfering genomes. *J Virol* **92**, e02094,
1755 10.1128/JVI.02094-17.
1756 77. Konno, Y., Kimura, I., Uriu, K., et al. (2020). SARS-CoV-2 ORF3b Is a
1757 Potent Interferon Antagonist Whose Activity Is Increased by a Naturally
1758 Occurring Elongation Variant. *Cell Rep* **32**, 108185,
1759 10.1016/j.celrep.2020.108185.
1760



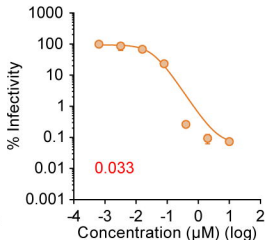
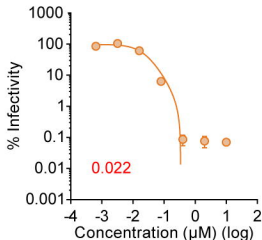
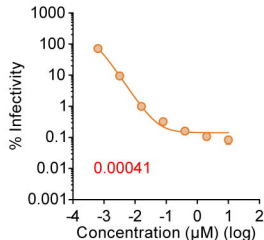


Nirmatrelvir

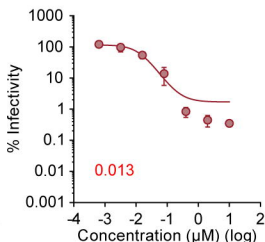
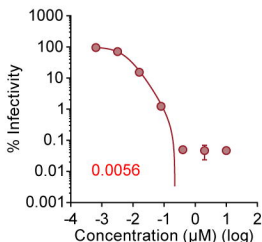
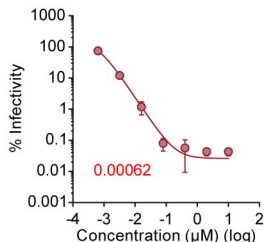
Remdesivir

Ensitrelvir

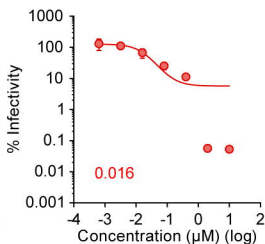
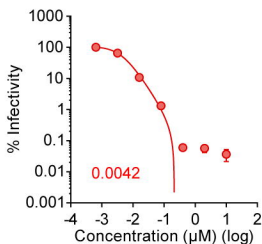
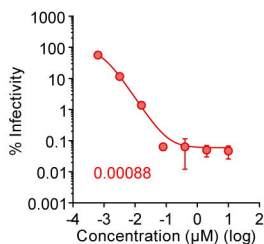
Delta



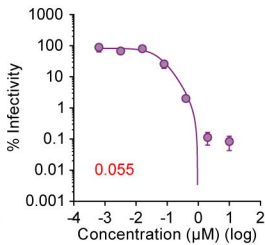
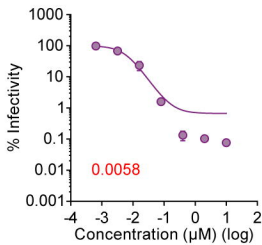
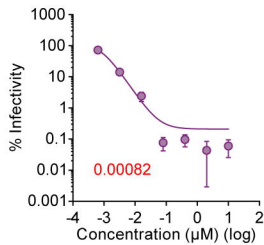
XBB.1.5

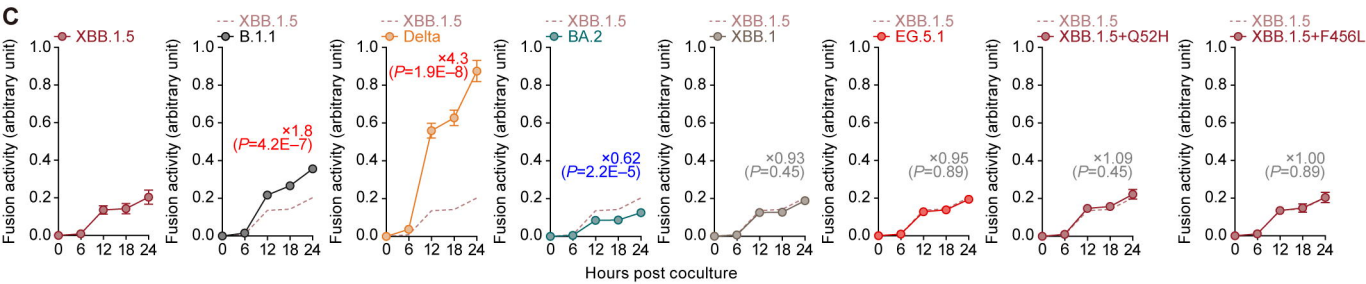
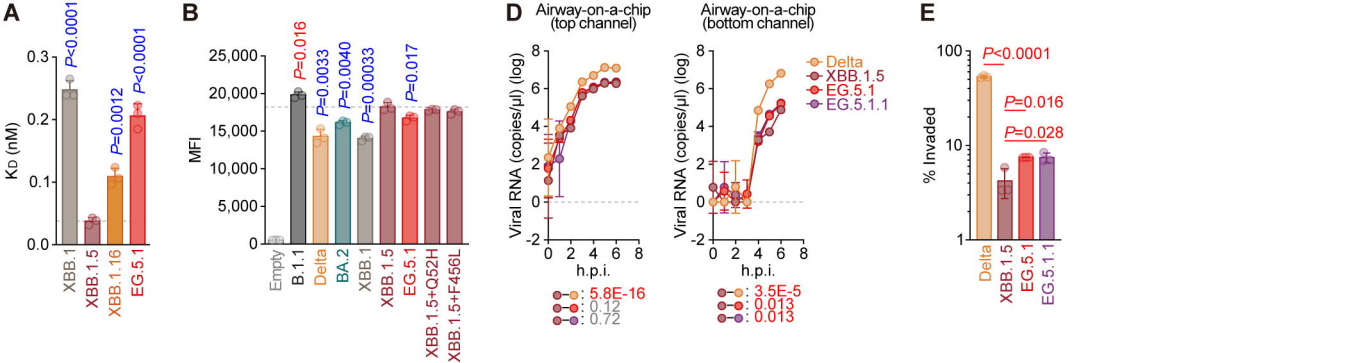


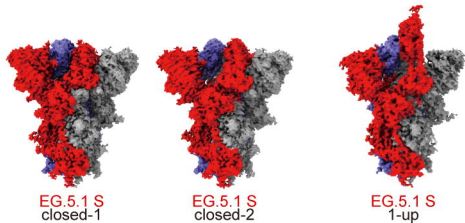
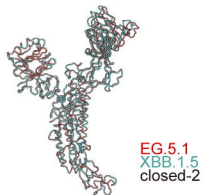
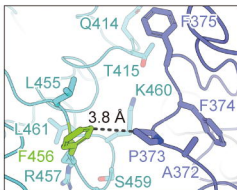
EG.5.1



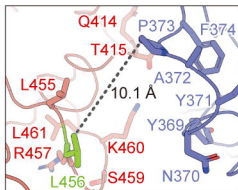
EG.5.1.1



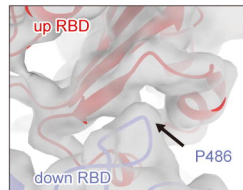


A**B****C**

XBB.1.5 closed-2



EG.5.1 S closed-2

D

EG.5.1 S 1-up

